Experimental Study of the HUM Control Operator for Linear Waves

Gilles Lebeau and Maëlle Nodet

CONTENTS

1. Introduction
2. Analysis of the Optimal Control Operator
3. Numerical Setup and Validation
4. Numerical Experiments
Acknowledgments
References

We consider the problem of the numerical approximation of the linear controllability of waves. All our experiments are done in a bounded domain Ω of the plane, with Dirichlet boundary conditions and internal control. We use a Galerkin approximation of the optimal control operator of the continuous model, based on the spectral theory of the Laplace operator in Ω. This allows us to obtain surprisingly good illustrations of the main theoretical results available on the controllability of waves and to formulate some questions for future analysis of the optimal control theory of waves.

1. INTRODUCTION

This paper is devoted to the experimental study of the exact controllability of waves. All our experiments will be done in a bounded domain Ω of the plane, with Dirichlet boundary conditions and with internal control. We use the most natural approach for the numerical computation: a Galerkin approximation of the optimal control operator of the continuous model based on the spectral theory of the Laplace operator in Ω. This will allow us to obtain surprisingly good illustrations of the main theoretical results available on the controllability of waves, and to formulate some questions for the future analysis of the optimal control theory of waves.

The problem of controllability for linear evolution equations and systems has a long history, for which we refer to the review in [Russell 78] and to the book [Lions 88]. Concerning controllability of linear waves, the main theoretical result is the so-called *geometric control condition* (GCC) from [Bardos et al. 92], which gives an (almost) necessary and sufficient condition for exact controllability. This is a "geometrical optics" condition on the behavior of optical rays inside $\overline{\Omega}$. Here, optical rays are just straight lines inside Ω, reflected at the boundary according to the Snell–Descartes law of reflection. The precise definition of optical rays near points of tangency

2000 AMS Subject Classification: Primary 35B37, 65-05, 35L05, 35A27

Keywords: Partial differential equations, optimal control, experimental mathematics, numerical analysis, microlocal analysis

with the boundary is given in [Melrose and Sjöstrand 78] and [Melrose and Sjöstrand 82].

For internal control, GCC asserts that waves in a regular bounded domain Ω are exactly controllable by control functions supported in the closure of an open subdomain U and acting during a time T if (and only if, if one allows arbitrarily small perturbations of the time control T and of the control domain U) the following condition holds:

> GCC: Every optical ray of length T in Ω enters the subdomain U.

Even when GCC is satisfied, the numerical computation of the control is not an easy task. The original approach consists first in discretizing the continuous model, and then in computing the control of the discrete system to use it as a numerical approximation of the continuous one. This method was developed by R. Glowinski et al. (see [Glowinski et al. 90] and [Glowinski et al. 08]) and used for numerical experiments in [Asch and Lebeau 98].

However, as observed in the first works of Glowinski, interaction of waves with a numerical mesh produces spurious high-frequency oscillations. In fact, the discrete model is not uniformly exactly controllable as the mesh size goes to zero, since the group velocity converges to zero when the solution's wavelength is comparable to the mesh size. In other words, the processes of numerical discretization and observation or control do not commute. A precise analysis of this lack of commutation and its impact on the computation of the control has been carried out in [Zuazua 02, Zuazua 05].

In this paper, we shall use another approach, namely, we will discretize the optimal control of the continuous model using a projection of the wave equation onto the finite-dimensional space spanned by the eigenfunctions e_j of the Laplace operator in Ω with Dirichlet boundary conditions $-\triangle e_j = \omega_j^2 e_j, e_j|_{\partial\Omega=0}$, with $\omega_j \leq \omega$. Here ω will be a cutoff frequency at our disposal. We prove (see Lemma 2.7 in Section 2.3) that when GCC is satisfied, our numerical control converges when $\omega \to \infty$ to the optimal control of the continuous model.

Moreover, when GCC is not satisfied, we will perform experiments in which we will see an exponential blowup in the cutoff frequency ω of the norm of the discretized optimal control. These blowup rates will be compared to theoretical results in Section 2.3.

The paper is organized as follows. Section 2 is devoted to the analysis of the optimal control operator for waves in a bounded regular domain of $\mathbb{R}^d$. In Section 2.1, we recall the definition of the optimal control operator Λ. In Section 2.2, we recall some known theoretical results on Λ: existence, regularity properties, and the fact that it preserves the frequency localization. We also state our first conjecture, namely that the optimal control operator Λ is a microlocal operator. In Section 2.3, we introduce the spectral Galerkin approximation $M_{T,\omega}^{-1}$ of Λ, where ω is a cutoff frequency. We prove the convergence of $M_{T,\omega}^{-1}$ toward Λ as $\omega \to \infty$, and we analyze the rate of this convergence. We also state our second conjecture on the blowup rate of $M_{T,\omega}^{-1}$ when GCC is not satisfied. Finally, in Section 2.4, we introduce the basis of the energy space in which we compute the matrix of the operator $M_{T,\omega}$.

Section 3 is devoted to the experimental validation of our Galerkin approximation. In Section 3.1 we introduce the three different domains of the plane for our experiments: square, disk, and trapezoid. In the first two cases, the geodesic flow is totally integrable, and the exact eigenfunctions and eigenvalues of the Laplace operator with Dirichlet boundary condition are known. This is not the case for the trapezoid.

In Section 3.2 we introduce the two different choices of the control operator we use in our experiments. In the first case (nonsmooth), we use $\chi(t,x) = \mathbf{1}_{[0,T]}\mathbf{1}_U$. In the second case (smooth), we use a suitable regularization of the first case (see (3–1) and (3–2)). Perhaps the main contribution of this paper is to give experimental evidence that the choice of a smooth enough control operator is the right way to obtain accuracy in control computing. In Section 3.3, in the two cases of the square and the disk, we compare the exact eigenvalues with the eigenvalues computed using the 5-point finite difference approximation of the Laplace operator. In Section 3.4, formula (3–3), we define the reconstruction error of our method.

Finally, in Section 3.5, in the case of the square geometry, we compare the control function (we choose to reconstruct a single eigenvalue) when the eigenvalues and eigenvectors are computed either with finite differences or with exact formulas, and we study the experimental convergence of our numerical optimal control to the exact optimal control of the continuous model as the cutoff frequency goes to infinity.

The last section, Section 4, presents various numerical experiments that illustrate the theoretical results of Section 2 and are in support of our two conjectures.

In Section 4.1, our experiments illuminate the fact that the optimal control operator preserves the frequency localization, and that this property is far stronger when the control function is smooth, as predicted by theoretical results. In Section 4.2, we use Dirac and box experiments

to illustrate the fact that the optimal control operator shows a behavior very close to that of a pseudodifferential operator: this is in support of our first conjecture. In Section 4.3, we plot the reconstruction error as a function of the cutoff frequency: this illuminates how the rate of convergence of the Galerkin approximation depends on the regularity of the control function. In Section 4.4, we present various results on the energy of the control function.

In Section 4.5, we compute the condition number of the matrix $M_{T,\omega}$ for a given control domain U as a function of the control time T and the cutoff frequency ω. In particular, Figures 30 and 31 are in support of our second conjecture on the blowup rate of $M_{T,\omega}^{-1}$ when GCC is not satisfied.

In Section 4.6, we perform experiments in the disk when GCC is not satisfied for two different data: In the first case, every optical ray of length T starting at a point where the data are not small enters the control domain U, and we observe a rather good reconstruction error if the cutoff frequency is not too high. In the second case, there exists an optical ray starting at a point where the data is not small and that never enters the control domain, and we observe a very poor reconstruction at any cutoff frequency.

This is a fascinating phenomenon that has not been previously studied in theoretical works. It will be of major practical interest to obtain quantitative results on the best cutoff frequency, the one that optimizes the reconstruction error (this optimal cutoff frequency is equal to ∞ when GCC is satisfied, the reconstruction error being equal to 0 in that case), and to estimate the reconstruction error at the optimal cutoff frequency. Clearly, our experiments indicate that a weak geometric control condition associated with the data one wants to reconstruct will enter into such a study.

2. ANALYSIS OF THE OPTIMAL CONTROL OPERATOR

2.1 The Optimal Control Operator

Here we recall the basic facts we will need in our study of the optimal control operator for linear waves. For more details on the Hilbert uniqueness method (HUM), we refer to [Lions 88].

In the framework of the wave equation in a bounded open subset Ω of $\mathbb{R}^d$ with boundary Dirichlet condition, and for internal control, the problem of controllability is stated in the following way: Let T be a positive time, U a nonempty open subset of Ω, and $\chi(t,x)$ as follows:

$$\chi(t,x) = \psi(t)\chi_0(x), \tag{2–1}$$

where χ_0 is a real L^∞ function on $\overline{\Omega}$ such that the support of (χ_0) equals $\overline{U}$ and $\chi_0(x)$ is continuous and positive for $x \in U$, $\psi \in C^\infty([0,T])$, and $\psi(t) > 0$ on $]0,T[$. For a given $f = (u_0, u_1) \in H_0^1(\Omega) \times L^2(\Omega)$, the problem is to find a source $v(t,x) \in L^2(0,T;L^2(\Omega))$ such that the solution of the system

$$\begin{aligned} \Box u &= \chi v \quad \text{in }]0,+\infty[\times\Omega, \\ u_{|\partial\Omega} &= 0, \quad t > 0, \\ (u|_{t=0}, \partial_t u|_{t=0}) &= (0,0), \end{aligned} \tag{2–2}$$

reaches the state $f = (u_0, u_1)$ at time T. We first rewrite the wave operator in (2–2) as a first-order system. Let A be the matrix

$$iA = \begin{pmatrix} 0 & \mathrm{Id} \\ \triangle & 0 \end{pmatrix}.$$

Then A is an unbounded self-adjoint operator on $H = H_0^1(\Omega) \times L^2(\Omega)$, where the scalar product on $H_0^1(\Omega)$ is $\int_\Omega \nabla u \overline{\nabla v}\, dx$ and $D(A) = \{\underline{u} = (u_0, u_1) \in H,\ A(\underline{u}) \in H,\ u_0|_{\partial\Omega} = 0\}$.

Let $\lambda = \sqrt{-\triangle_D}$, where $-\triangle_D$ is the canonical isomorphism from $H_0^1(\Omega)$ onto $H^{-1}(\Omega)$; λ is an isomorphism from $H_0^1(\Omega)$ onto $L^2(\Omega)$. The operator $B(t)$ given by

$$B(t) = \begin{pmatrix} 0 & 0 \\ \chi(t,\cdot)\lambda & 0 \end{pmatrix}$$

is bounded on H, and one has

$$B^*(t) = \begin{pmatrix} 0 & \lambda^{-1}\chi(t,\cdot) \\ 0 & 0 \end{pmatrix}. \tag{2–3}$$

The system (2–2) is then equivalent to

$$(\partial_t - iA)f = B(t)g, \quad f(0) = 0,$$

with $f = (u, \partial_t u)$, $g = (\lambda^{-1}v, 0)$. For any $g(t) \in L^1([0,\infty[, H)$, the evolution equation

$$(\partial_t - iA)f = B(t)g, \quad f(0) = 0,$$

admits a unique solution $f = S(g) \in C^0([0,+\infty[, H)$ given by the Duhamel formula

$$f(t) = \int_0^t e^{i(t-s)A} B(s)g(s)\, ds.$$

Let $T > 0$ be given. Let $\mathcal{R}_T$ be the reachable set at time T. Then

$$\mathcal{R}_T = \{f \in H \mid \exists g \in L^2([0,T], H) \text{ s.t. } f = S(g)(T)\}.$$

Then $\mathcal{R}_T$ is a linear subspace of H and is the set of states of the system that one can reach in time T, starting from rest, with the action of an L^2 source g filtered by the control operator B. The control problem consists in giving an accurate description of $\mathcal{R}_T$, and exact controllability is equivalent to the equality $\mathcal{R}_T = H$. Let us recall some basic facts.

Let $\mathcal{H} = L^2([0,T], H)$. Let $\mathcal{F}$ be the closed subspace of $\mathcal{H}$ spanned by solutions of the adjoint evolution equation

$$\mathcal{F} = \{h \in \mathcal{H} \mid (\partial_t - iA^*)h = 0,\ h(T) = h_T \in H\}. \quad (2\text{–}4)$$

Observe that in our context, $A^* = A$, and the function h in (2–4) is given by $h(t) = e^{-i(T-t)A}h_T$. Let $\mathcal{B}^*$ be the adjoint of the operator $g \mapsto S(g)(T)$. Then $\mathcal{B}^*$ is the bounded operator from H into $\mathcal{H}$ defined by

$$\mathcal{B}^*(h_T)(t) = B^*(t)e^{-i(T-t)A}h_T.$$

For any $g \in L^2([0,T], H)$, one has, with $f_T = S(g)(T)$ and $h(s) = e^{-i(T-s)A}h_T$, the fundamental identity

$$(f_T|h_T)_H = \int_0^T (B(s)g(s)|h(s))ds = (g|\mathcal{B}^*(h_T))_{\mathcal{H}}. \quad (2\text{–}5)$$

From (2–5), one easily obtains that

$$\mathcal{R}_T \text{ is a dense subspace of } H \iff \mathcal{B}^* \text{ is an injective operator,}$$

which shows that approximate controllability is equivalent to a uniqueness result on the adjoint equation. Moreover, one gets from (2–5), using the Riesz and closed graph theorems, that

$$\mathcal{R}_T = H \iff \exists C \text{ s.t. } \|h\| \le C\|\mathcal{B}^*h\|\ \forall h \in H. \quad (2\text{–}6)$$

This is an observability inequality, and $\mathcal{B}^*$ is called the observability operator. We rewrite the observability inequality (2–6) in a more explicit form:

$$\exists C \text{ s.t. } \|h\|_H^2 \le C\int_0^T \|B^*(s)e^{-i(T-s)A}h\|_H^2\, ds\ \forall h \in H. \quad (2\text{–}7)$$

Assuming that (2–7) holds, then $\mathcal{R}_T = H$, $\mathrm{Im}(\mathcal{B}^*)$ is a closed subspace of $\mathcal{H}$, and $\mathcal{B}^*$ is an isomorphism of H onto $\mathrm{Im}(\mathcal{B}^*)$. For any $f \in H$, let $\mathcal{C}_f$ be the set of control functions g driving 0 to f in time T:

$$\mathcal{C}_f = \Big\{g \in L^2([0,T], H),\ f = \int_0^T e^{i(T-s)A}B(s)g(s)\, ds\Big\}.$$

From (2–5), one gets

$$\mathcal{C}_f = g_0 + (\mathrm{Im}\mathcal{B}^*)^\perp, \quad g_0 \in \mathrm{Im}\mathcal{B}^* \cap \mathcal{C}_f,$$

and $g_0 = \mathcal{B}^*h_T$ is the optimal control in the sense that

$$\min\{\|g\|_{L^2([0,T],H)}, g \in \mathcal{C}_f\} \text{ is achieved at } g = g_0.$$

Let $\Lambda : H \to H$, $\Lambda(f) = h_T$, be the control map, so that the optimal control g_0 is equal to $g_0(t) = B^*(t)e^{-i(T-t)A}\Lambda(f)$. Then Λ is exactly the inverse of the map $M_T : H \to H$ with

$$M_T = \int_0^T m(T-t)dt = \int_0^T m(s)ds, \quad (2\text{–}8)$$
$$m(s) = e^{isA}B(T-s)B^*(T-s)e^{-isA^*}.$$

Observe that $m(s) = m^*(s)$ is a bounded self-adjoint nonnegative operator on H. Exact controllability is thus equivalent to the existence of $C > 0$ such that

$$M_T = \int_0^T e^{i(T-t)A}\begin{pmatrix} 0 & 0 \\ 0 & \chi^2(t,\cdot)\end{pmatrix}e^{-i(T-t)A}dt \ge C\,\mathrm{Id}. \quad (2\text{–}9)$$

With $\Lambda = M_T^{-1}$, the optimal control is then given by $g_0(t) = B^*(t)e^{-i(T-t)A}\Lambda(f)$ and is by (2–3) of the form $g_0 = (\lambda^{-1}\chi\partial_t w, 0)$, where $w(t) = e^{-i(T-t)A}\Lambda(f)$ is the solution of

$$\begin{aligned} \Box w &= 0 \quad \text{in } \mathbb{R}\times\Omega, \\ w_{|\partial\Omega} &= 0, \\ (w(t,\cdot), \partial_t w(t,\cdot)) &= \Lambda(f). \end{aligned} \quad (2\text{–}10)$$

Thus, the optimal control function v in (2–2) is equal to $v = \chi\partial_t w$, where w is the solution of the dual problem (2–10). The operator $\Lambda = M_T^{-1}$, with M_T given by (2–9), is called the optimal control operator.

2.2 Theoretical Results

In this section we recall some theoretical results on the analysis of the optimal control operator Λ. We will assume here that Ω is a bounded open subset of $\mathbb{R}^d$ with smooth boundary $\partial\Omega$, and that any straight line in $\mathbb{R}^d$ has only finite order of contacts with the boundary. In that case, optical rays are uniquely defined. See an example of such rays in Figure 1.

Let $M = \Omega \times \mathbb{R}_t$. The phase space is

$${}^bT^*M = T^*\overline{M} \setminus T^*_{\partial M} \simeq T^*M \cup T^*\partial M.$$

The characteristic variety of the wave operator is the closed subset Σ of ${}^bT^*M$ of points (x,t,ξ,τ) such that $|\tau| = |\xi|$ when $x \in \Omega$ and $|\tau| \ge |\xi|$ when $x \in \partial\Omega$. Let ${}^bS^*\overline{\Omega}$ be the set of points

$${}^bS^*\overline{\Omega} = \{(x_0, \xi_0),\},$$

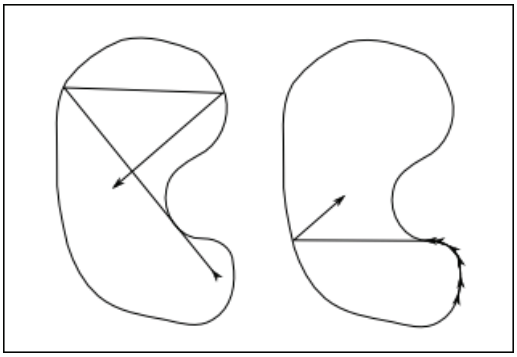

FIGURE 1. Example of optical rays.

where

$$|\xi_0| = 1 \text{ if } x_0 \in \Omega, \quad |\xi_0| \leq 1 \text{ if } x_0 \in \partial\Omega.$$

For $\rho_0 = (x_0, \xi_0) \in {}^bS^*\overline{\Omega}$ and $\tau = \pm 1$, we shall denote by $s \to (\gamma_{\rho_0}(s), t - s\tau, \tau)$, $s \in \mathbb{R}$, the generalized bicharacteristic ray of the wave operator, issued from (x_0, ξ_0, t, τ). For the construction of the Melrose–Sjöstrand flow, we refer to [Melrose and Sjöstrand 78, Melrose and Sjöstrand 82] and to [Hörmander 85, vol. 3, Chapter XXIV].

Then $s \to \gamma_{\rho_0}(s) = (x(\rho_0, s), \xi(\rho_0, s))$ is the optical ray starting at x_0 in the direction ξ_0. When $x_0 \in \partial\Omega$ and $|\xi_0| < 1$, then the right (respectively left) derivative of $x(\rho_0, s)$ at $s = 0$ is equal to the unit vector in $\mathbb{R}^d$ that projects onto $\xi_0 \in T^*\partial\Omega$ and that points inside (respectively outside) Ω. In all other cases, $x(\rho_0, s)$ is differentiable at $s = 0$ with derivative equal to ξ_0.

We first recall the theorem of [Bardos et al. 92], which gives the existence of the operator Λ:

Theorem 2.1. *If the geometric control condition holds, then M_T is an isomorphism.*

Next, we recall some new theoretical results obtained in [Dehman and Lebeau 09]. For these results, the choice of the control function $\chi(t, x)$ in (2–1) will be essential.

Definition 2.2. The control function $\chi(t, x) = \psi(t)\chi_0(x)$ is *smooth* if $\chi_0 \in C^\infty(\overline{\Omega})$ and $\psi(t)$ is flat at $t = 0$ and $t = T$.

For $s \in \mathbb{R}$, we denote by $H^s(\Omega, \triangle)$ the domain of the operator $(-\triangle_{\text{Dirichlet}})^{s/2}$. One has $H^0(\Omega, \triangle) = L^2(\Omega)$, $H^1(\Omega, \triangle) = H_0^1(\Omega)$, and if $(e_j)_{j\geq 1}$ is an L^2 orthonormal basis of eigenfunctions of $-\triangle$ with Dirichlet boundary conditions, $-\triangle e_j = \omega_j^2 e_j$, $0 < \omega_1 \leq \omega_2 \leq \cdots$, one has

$$H^s(\Omega, \triangle) = \Big\{ f \in \mathcal{D}'(\Omega), f = \sum_j f_j e_j, \ \sum_j \omega_j^{2s} |f_j|^2 < \infty \Big\}. \tag{2–11}$$

The following result of [Dehman and Lebeau 09] says that under the hypothesis that the control function $\chi(t, x)$ is smooth, the optimal control operator Λ preserves the regularity described in the following theorem.

Theorem 2.3. *Assume that the geometric control condition holds, and that the control function $\chi(t, x)$ is smooth. Then the optimal control operator Λ is an isomorphism of $H^{s+1}(\Omega, \Delta) \oplus H^s(\Omega, \Delta)$ for all $s \geq 0$.*

Observe that Theorem 2.1 is a particular case of Theorem 2.3 with $s = 0$. In our experimental study, we will see in Section 4.3 that the regularity of the control function $\chi(t, x)$ is not only a nice hypothesis for obtaining theoretical results. It is also very efficient for achieving accuracy in the numerical computation of the control function. In other words, the usual choice of the control function $\chi(t, x) = \mathbf{1}_{[0,T]}\mathbf{1}_U$ is a very poor one for computing a control.

The next result states that the optimal control operator Λ preserves the frequency localization. To state this result, we briefly introduce the material needed for the Littlewood–Paley decomposition. Let $\phi \in C^\infty([0, \infty[)$, with $\phi(x) = 1$ for $|x| \leq 1/2$ and $\phi(x) = 0$ for $|x| \geq 1$. Set $\psi(x) = \phi(x) - \phi(2x)$. Then $\psi \in C_0^\infty(\mathbb{R}^*)$, ψ vanishes outside $[1/4, 1]$, and one has

$$\phi(s) + \sum_{k=1}^{\infty} \psi(2^{-k}s) = 1, \quad \forall s \in [0, \infty[\,.$$

Set $\psi_0(s) = \phi(s)$ and $\psi_k(s) = \psi(2^{-k}s)$ for $k \geq 1$. We then define the spectral localization operators $\psi_k(D)$, $k \in \mathbb{N}$, in the following way: for $u = \sum_j a_j e_j$, we define

$$\psi_k(D)u = \sum_j \psi_k(\omega_j) a_j e_j.$$

One has $\sum_k \psi_k(D) = \mathrm{Id}$ and $\psi_i(D)\psi_j(D) = 0$ for $|i-j| \geq 2$. In addition, we introduce

$$S_k(D) = \sum_{j=0}^{k} \psi_j(D) = \psi_0(2^{-k}D), \quad k \geq 0.$$

Obviously, the operators $\psi_k(D)$ and $S_k(D)$ act as bounded operators on $H = H_0^1 \times L^2$. The spectral localization result of [Dehman and Lebeau 09] reads as follows.

Theorem 2.4. *Assume that the geometric control condition holds, and that the control function $\chi(t,x)$ is smooth. Then there exists $C>0$ such that for every $k\in\mathbb{N}$, the following inequalities hold:*

$$\|\psi_k(D)\Lambda-\Lambda\psi_k(D)\|_H\le C2^{-k},$$
$$\|S_k(D)\Lambda-\Lambda S_k(D)\|_H\le C2^{-k}$$

Theorem 2.4 states that the optimal control operator Λ, up to lower-order terms, acts individually on each frequency block of the solution. For instance, if e_n is the nth eigenvector of the orthonormal basis of $L^2(\Omega)$ and if one drives the data $(0,0)$ to $(e_n,0)$ in (2–2) using the optimal control, then both the solution u and control v in (2–2) will essentially live at frequency ω_n for n large. We shall do experiments on this fact in Section 4.1, and we will clearly see the impact of the regularity of the control function $\chi(t,x)$ on the accuracy of the frequency localization of the numerical control.

Since by the above results the optimal control operator Λ preserves the regularity and the frequency localization, it is very natural to expect that Λ is in fact a microlocal operator, and in particular preserves the wave-front set. For an introduction to microlocal analysis and pseudodifferential calculus, we refer to [Taylor 81, Hörmander 85]. In [Dehman and Lebeau 09], it is proved that the optimal control operator Λ for waves on a compact Riemannian manifold without boundary is in fact an elliptic 2×2 matrix of pseudodifferential operators.

This is quite an easy result, since if $\chi(t,x)$ is smooth, Egorov's theorem implies that the operator M_T given by (2–9) is a 2×2 matrix of pseudodifferential operators. Moreover, the geometric control condition implies easily that M_T is elliptic. Since M_T is self-adjoint, the fact that M_T is an isomorphism follows from $\mathrm{Ker}(M_T)=\{0\}$, which is equivalent to the injectivity of $\mathcal{B}^*$. This is proved in [Bardos et al. 92] as a consequence of the uniqueness theorem of Calderón for the elliptic second-order operator $\triangle$. Then it follows that its inverse $\Lambda=M_T^{-1}$ is an elliptic pseudodifferential operator.

In our context, for waves in a bounded regular open subset Ω of $\mathbb{R}^d$ with boundary Dirichlet condition, the situation is far more complicated, since there is no Egorov theorem in the geometric setting of a manifold with boundary. In fact, the Melrose–Sjöstrand theorem [Melrose and Sjöstrand 78, Melrose and Sjöstrand 82] on propagation of singularities at the boundary (see also [Hörmander 85, vol. 3, Chapter XXIV] for a proof) implies that the operator M_T given by (2–9) is a microlocal operator, but this is insufficient to imply that its inverse Λ is microlocal.

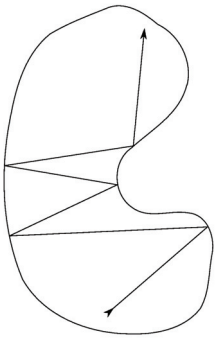

FIGURE 2. Example of optical ray with only transversal reflection points.

However, let $\rho_0=(x_0,\xi_0)\in T^*\Omega, |\xi_0|=1$ be a point in the cotangent space such that the two optical rays defined by the Melrose–Sjöstrand flow (see [Melrose and Sjöstrand 78, Melrose and Sjöstrand 82]) $s\in[0,T]\to\gamma_{\pm\rho_0}(s)=(x(\pm\rho_0,s),\xi(\pm\rho_0,s))$, with $\pm\rho_0=(x_0,\pm\xi_0)$, starting at x_0 in the directions $\pm\xi_0$ have only transversal intersections with the boundary. Then it is not hard to show using (2–9) and the parametrix of the wave operator, inside Ω and near transversal reflection points at the boundary $\partial\Omega$, as presented in Figure 2, that M_T is microlocally at ρ_0 an elliptic 2×2 matrix of elliptic pseudodifferential operators.

More precisely, let J be the isomorphism from $H_0^1\oplus L^2$ on $L^2\oplus L^2$ given by

$$J=\frac{1}{2}\begin{pmatrix}\lambda & -i\\ \lambda & i\end{pmatrix}.$$

One has $2\|J\underline{u}\|^2_{L^2\oplus L^2}=\|\underline{u}\|^2_{H_0^1\oplus L^2}$, and if $u(t,x)$ is the solution of the wave operator $\Box u=0$ with Dirichlet boundary conditions on $\partial\Omega$, and Cauchy data at time t_0 equal to (u_0,u_1), then one has

$$\begin{aligned}\lambda u(t,\cdot)&=\lambda\cos((t-t_0)\lambda)u_0+\sin((t-t_0)\lambda)u_1\\&=e^{i(t-t_0)\lambda}\Big(\frac{\lambda u_0-iu_1}{2}\Big)+e^{-i(t-t_0)\lambda}\Big(\frac{\lambda u_0+iu_1}{2}\Big),\end{aligned}$$

so the effect of the isomorphism J is to split the solution $u(t,x)$ into a sum of two waves with positive and negative temporal frequencies. Moreover, one has

$$Je^{itA}J^{-1}=\begin{pmatrix}e^{it\lambda} & 0\\ 0 & e^{-it\lambda}\end{pmatrix}.$$

Then JM_TJ^{-1} acts as a nonnegative self-adjoint operator on $L^2 \oplus L^2$, and is equal to

$$JM_TJ^{-1} = \frac{1}{2}\begin{pmatrix} Q_+ & -\mathcal{T} \\ -\mathcal{T}^* & Q_- \end{pmatrix},$$
$$Q_\pm = \int_0^T e^{\pm is\lambda}\chi^2(T-s,.)e^{\mp is\lambda}ds, \qquad (2\text{–}12)$$
$$\mathcal{T} = \int_0^T e^{is\lambda}\chi^2(T-s,.)e^{is\lambda}ds.$$

From (2–12), using the parametrix of the wave operator inside Ω and near transversal reflection points at the boundary $\partial\Omega$, and integration by parts to show that $\mathcal{T}$ is a smoothing operator, it is not difficult to obtain that JM_TJ^{-1} is microlocally at $\rho_0 \in T^*\Omega$ a pseudodifferential operator of order zero with principal symbol

$$\sigma_0(JM_TJ^{-1})(\rho_0) = \frac{1}{2}\begin{pmatrix} q_+(x_0,\xi_0) & 0 \\ 0 & q_-(x_0,\xi_0) \end{pmatrix},$$
$$q_\pm(x_0,\xi_0) = \int_0^T \chi^2(T-s, x(\pm\rho_0,s))ds. \quad (2\text{–}13)$$

Obviously, this condition guarantees that $\sigma_0(JM_TJ^{-1})(\rho_0)$ is elliptic, and therefore $J\Lambda J^{-1}$ will be at ρ_0 a pseudodifferential operator of order zero with principal symbol

$$\sigma_0(J\Lambda J^{-1})(\rho_0) = 2\begin{pmatrix} q_+^{-1}(x_0,\xi_0) & 0 \\ 0 & q_-^{-1}(x_0,\xi_0) \end{pmatrix}. \qquad (2\text{–}14)$$

Therefore, the only difficulty in order to prove that Λ is a microlocal operator is to obtain a precise analysis of the structure of the operator M_T near rays that are tangent to the boundary. Since the set of $\rho \in^b S^*\overline{\Omega}$ for which the optical ray $\gamma_\rho(s)$ has only transversal points of intersection with the boundary is dense in $T^*\overline{\Omega}\setminus T^*_{\partial\Omega}$ (see [Hörmander 85]), it is not surprising that our numerical experiments in Section 4.2 (where we compute the optimal control associated with a Dirac mass $\delta_{x_0}, x_0 \in \Omega$) confirms the following conjecture:

Conjecture 2.5. *Assume that the geometric control condition holds, that the control function $\chi(t,x)$ is smooth, and that the optical rays have no infinite order of contact with the boundary. Then Λ is a microlocal operator.*

Of course, part of the difficulty is to define correctly what a microlocal operator is in our context. In the above conjecture, microlocal implies in particular that the optimal control operator Λ preserves the wave-front set. A far less precise piece of information is that Λ is a microlocal operator at the level of microlocal defect measures, for which we refer to [Gérard 91]. But this is an easy byproduct of the result of [Burq and Lebeau 01].

2.3 The Spectral Galerkin Method

In this section we describe our numerical approximation of the optimal control operator Λ, and we give some theoretical results on the numerical approximation $M_{T,\omega}$ of the operator M_T given by (2–9), even in the case in which the geometric control condition is not satisfied.

For any cutoff frequency ω, we denote by Π_ω the orthogonal projection, in the Hilbert space $L^2(\Omega)$, onto the finite-dimensional linear subspace L^2_ω spanned by the eigenvectors e_j for $\omega_j \le \omega$. By the Weyl formula, if c_d denotes the volume of the unit ball in $\mathbb{R}^d$, one has

$$N(\omega) = \dim(L^2_\omega) \simeq (2\pi)^{-d}\,\mathrm{Vol}(\Omega)c_d\omega^d \quad (\omega \to +\infty).$$

Obviously, Π_ω acts on $H = H^1_0 \times L^2$ and commutes with e^{itA}, λ, and J. We define the Galerkin approximation $M_{T,\omega}$ of the operator M_T as the following operator on $L^2_\omega \times L^2_\omega$:

$$M_{T,\omega} = \Pi_\omega M_T \Pi_\omega$$
$$= \int_0^T e^{i(T-t)A}\Pi_\omega \begin{pmatrix} 0 & 0 \\ 0 & \chi^2(t,\cdot) \end{pmatrix} \Pi_\omega e^{-i(T-t)A}dt.$$

Obviously, the matrix $M_{T,\omega}$ is symmetric and nonnegative for the Hilbert structure induced by H on $L^2_\omega \times L^2_\omega$, and by (2–8) one has with $n_\omega(t) = B^*(t)\Pi_\omega e^{-i(T-t)A}$,

$$M_{T,\omega} = \int_0^T n^*_\omega(t)n_\omega(t)\,dt. \qquad (2\text{–}15)$$

By (2–12) one has also

$$JM_{T,\omega}J^{-1} = \frac{1}{2}\begin{pmatrix} Q_{+,\omega} & -\mathcal{T}_\omega \\ -\mathcal{T}^*_\omega & Q_{-,\omega} \end{pmatrix}, \qquad (2\text{–}16)$$
$$Q_{\pm,\omega} = \int_0^T e^{\pm is\lambda}\Pi_\omega\chi^2(T-s,.)\Pi_\omega e^{\mp is\lambda}ds,$$
$$\mathcal{T}_\omega = \int_0^T e^{is\lambda}\Pi_\omega\chi^2(T-s,.)\Pi_\omega e^{is\lambda}ds.$$

Let us first recall two easy results. For convenience, we recall here the proof of these results. The first states that the matrix $M_{T,\omega}$ is always invertible.

Lemma 2.6. *For any (nonzero) control function $\chi(t,x)$, the matrix $M_{T,\omega}$ is invertible.*

Proof: Let $u = (u_0,u_1) \in L^2_\omega \times L^2_\omega$ be such that $M_{T,\omega}(u) = 0$. By (2–15) one has

$$0 = (M_{T,\omega}(u)|u)_H = \int_0^T \|n_\omega(t)(u)\|^2_H dt.$$

This implies $n_\omega(t)(u) = 0$ for almost all $t \in]0,T[$. If $u(t,x)$ is the solution of the wave equation with Cauchy data (u_0,u_1) at time T, we thus get by (2–3) and (2–1) that $\psi(t)\chi_0(x)\partial_t u(t,x) = 0$ for $t \in [0,T]$, and since $\psi(t) > 0$ on $]0,T[$ and $\chi_0(x) > 0$ on U, we obtain $\partial_t u(t,x) = 0$ on $]0,T[\times U$. One has $u_0 = \sum_{\omega_j \le \omega} a_j e_j(x)$, $u_1 = \sum_{\omega_j \le \omega} b_j e_j(x)$, and

$$\partial_t u(t,x) = \sum_{\omega_j \le \omega} \omega_j a_j \sin((T-t)\omega_j) e_j(x) + \sum_{\omega_j \le \omega} b_j \cos((T-t)\omega_j) e_j(x).$$

Thus we obtain $\sum_{\omega_j \le \omega} \omega_j a_j e_j(x) = \sum_{\omega_j \le \omega} b_j e_j(x) = 0$ for $x \in U$, which implies, since the eigenfunctions e_j are analytic in Ω, that $a_j = b_j = 0$ for all j. □

For any $\omega_0 \le \omega$, we define $\Pi_\omega^\perp = 1 - \Pi_\omega$, and we set

$$\|\Pi_\omega^\perp \Lambda \Pi_{\omega_0}\|_H = r_\Lambda(\omega,\omega_0), \qquad \|\Pi_\omega^\perp M_T \Pi_{\omega_0}\|_H = r_M(\omega,\omega_0). \tag{2–17}$$

Since the ranges of the operators $\Lambda\Pi_{\omega_0}$ and $M_T\Pi_{\omega_0}$ are finite-dimensional vector spaces, one has for any ω_0,

$$\lim_{\omega\to\infty} r_\Lambda(\omega,\omega_0) = 0, \qquad \lim_{\omega\to\infty} r_M(\omega,\omega_0) = 0. \tag{2–18}$$

The second result states that when GCC holds, the inverse matrix $M_{T,\omega}^{-1}$ converges in the proper sense to the optimal control operator Λ as the cutoff frequency ω goes to infinity.

Lemma 2.7. *Assume that the geometric condition holds. Then there exists $c > 0$ such that we have the following: For any given $f \in H$, let $g = \Lambda(f)$, $f_\omega = \Pi_\omega f$, and $g^\omega = M_{T,\omega}^{-1}(f_\omega)$. Then one has*

$$\|g - g^\omega\|_H \le c\|f - f_\omega\|_H + \|\Lambda(f_\omega) - M_{T,\omega}^{-1}(f_\omega)\|_H \tag{2–19}$$

with

$$\lim_{\omega\to\infty} \|\Lambda(f_\omega) - M_{T,\omega}^{-1}(f_\omega)\|_H = 0. \tag{2–20}$$

Proof: Since GCC holds, there exists $C > 0$ such that by (2–9), one has $(M_T u|u)_H \ge C\|u\|_H^2$ for all $u \in H$, and hence $(M_{T,\omega}u|u)_H \ge C\|u\|_H^2$ for all $u \in L^2_\omega \times L^2_\omega$. Thus, with $c = C^{-1}$, one has $\|\Lambda\|_H \le c$ and $\|M_{T,\omega}^{-1}\|_H \le c$ for all ω. Since $g - g^\omega = \Lambda(f - f_\omega) + \Lambda(f_\omega) - M_{T,\omega}^{-1} f_\omega$, we have (2–19). Let us prove that (2–20) holds as well.

With $\Lambda_\omega = \Pi_\omega \Lambda \Pi_\omega$, one has

$$\Lambda(f_\omega) - M_{T,\omega}^{-1}(f_\omega) = \Pi_\omega^\perp \Lambda(f_\omega) + (\Lambda_\omega - M_{T,\omega}^{-1}) f_\omega. \tag{2–21}$$

Set for $\omega_0 \le \omega$, $f_{\omega_0,\omega} = (\Pi_\omega - \Pi_{\omega_0}) f$. Then one has

$$\begin{aligned}\|\Pi_\omega^\perp \Lambda(f_\omega)\|_H &= \|\Pi_\omega^\perp \Lambda \Pi_{\omega_0}(f) + \Pi_\omega^\perp \Lambda(f_{\omega_0,\omega})\|_H \\ &\le r_\Lambda(\omega,\omega_0)\|f\|_H + c\|f_{\omega_0,\omega}\|_H. \end{aligned}\tag{2–22}$$

On the other hand, one has

$$\begin{aligned}(\Lambda_\omega - M_{T,\omega}^{-1}) f_\omega &= M_{T,\omega}^{-1}(\Pi_\omega M_T \Pi_\omega^2 \Lambda - \Pi_\omega) f_\omega \\ &= M_{T,\omega}^{-1}(\Pi_\omega M_T \Pi_\omega - \Pi_\omega M_T)\Lambda f_\omega \\ &= -M_{T,\omega}^{-1} \Pi_\omega M_T \Pi_\omega^\perp \Lambda \Pi_\omega f. \end{aligned}\tag{2–23}$$

From (2–23) we get

$$\begin{aligned}&\|(\Lambda_\omega - M_{T,\omega}^{-1}) f_\omega\|_H \\ &\quad \le c\|M_T\|(\|\Lambda\|\|f_{\omega_0,\omega}\|_H + r_\Lambda(\omega,\omega_0)\|f\|_H). \end{aligned}\tag{2–24}$$

Thus, for all $\omega_0 \le \omega$, we get from (2–22), (2–24), and (2–21) that

$$\begin{aligned}&\|\Lambda(f_\omega) - M_{T,\omega}^{-1}(f_\omega)\|_H \\ &\quad \le (1 + c\|M_T\|)\Big(r_\Lambda(\omega,\omega_0)\|f\|_H + c\|f_{\omega_0,\omega}\|_H\Big), \end{aligned}\tag{2–25}$$

and (2–20) follows from (2–18), (2–25), and $\|f_{\omega_0,\omega}\|_H \le \|\Pi_{\omega_0}^\perp f\|_H \to 0$ as $\omega_0 \to \infty$. □

We shall now discuss two important points linked to the previous lemmas. The first is about the growth of the function

$$\omega \to \|M_{T,\omega}^{-1}\|_H$$

as $\omega \to \infty$. This function is bounded when the geometric control condition is satisfied. Let us recall some known results in the general case. For simplicity, we assume that $\partial\Omega$ is an analytic hypersurface of $\mathbb{R}^d$. We know from [Lebeau 92] that for $T > T_u$, where $T_u = 2\sup_{x\in\Omega} \mathrm{dist}_\Omega(x,U)$ is the uniqueness time, there exists $A > 0$ such that

$$\limsup_{\omega\to\infty} \frac{\log \|M_{T,\omega}^{-1}\|_H}{\omega} \le A.$$

On the other hand, when there exists $\rho_0 \in T^*\Omega$ such that the optical ray $s \in [0,T] \to \gamma_{\rho_0}(s)$ has only transversal points of intersection with the boundary and is such that $x(\rho_0,s) \notin \overline{U}$ for all $s \in [0,T]$, then GCC is not satisfied. Moreover, it is proven in [Lebeau 92], using an explicit construction of a wave concentrated near this optical ray, that there exists $B > 0$ such that

$$\liminf_{\omega\to\infty} \frac{\log \|M_{T,\omega}^{-1}\|_H}{\omega} \ge B.$$

Our experiments lead us to believe that the following conjecture may be true for a "generic" choice of the control function $\chi(t,x)$:

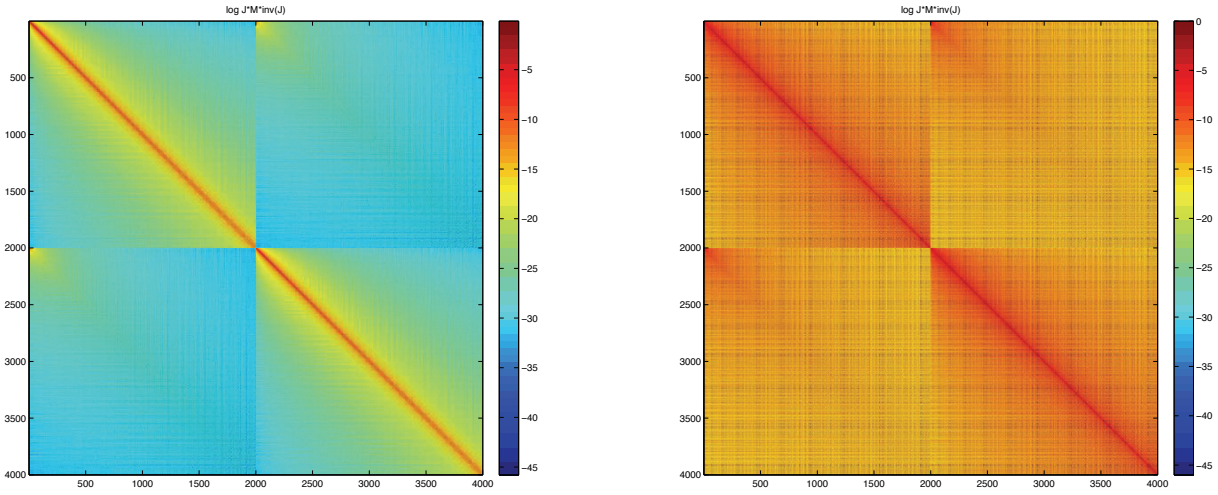

FIGURE 3. View of the logarithm of the coefficients of the matrix JM_TJ^{-1}, for the square geometry, with smooth control (left) and nonsmooth control (right). Note that the color scaling is the same. This illustrates decay estimates (2–26) and (2–27).

Conjecture 2.8. *There exists $C(T,U)$ such that*

$$\lim_{\omega\to\infty} \frac{\log \|M_{T,\omega}^{-1}\|_H}{\omega} = C(T,U).$$

In our experiments, we have studied (see Section 4.5) the behavior of $C(T,U)$ as a function of T when the geometric control condition is satisfied for the control domain U for $T \geq T_0$. These experiments confirm Conjecture 2.8 when $T < T_0$. We have not seen any clear change in the behavior of the constant $C(T,U)$ when T is smaller than the uniqueness time T_u.

The second point we shall discuss is the rate of convergence of our Galerkin approximation. By Lemma 2.7 and formulas (2–24) and (2–25), this speed of convergence is governed by the function $r_\Lambda(\omega,\omega_0)$ defined in (2–17). The following lemma tells us that when the control function is smooth, the convergence in (2–18) is very fast.

Lemma 2.9. *Assume that GCC holds and that the control function $\chi(t,x)$ is smooth. Then there exists a function g with rapid decay such that*

$$r_\Lambda(\omega,\omega_0) \leq g\left(\frac{\omega}{\omega_0}\right).$$

Proof: By Theorem 2.3, the operator $\lambda^s\Lambda\lambda^{-s}$ is bounded on H for all $s \geq 0$. Thus we obtain, for all $s \geq 0$,

$$\|\Pi_\omega^\perp \Lambda \Pi_{\omega_0}\|_H = \|\Pi_\omega^\perp \lambda^{-s}\lambda^s\Lambda\lambda^{-s}\lambda^s\Pi_{\omega_0}\|_H \leq C_s\left(\frac{\omega_0}{\omega}\right)^s,$$

where we have used $\|\lambda^s\Pi_{\omega_0}\|_H \leq \omega_0^s$ and $\|\Pi_\omega^\perp\lambda^{-s}\|_H \leq \omega^{-s}$. The proof of Lemma 2.9 is complete. □

Let us recall that $JM_{T,\omega}J^{-1}$ and that the operators $Q_{\pm,\omega}$ and $\mathcal{T}_\omega$ are defined by (2–16). For any bounded operator M on L^2, the matrix coefficients of M in the basis of the eigenvectors e_n are

$$M_{i,j} = (Me_i \mid e_j).$$

From (2–1) and (2–16) one has, for $\omega_i \leq \omega$, $\omega_j \leq \omega$,

$$\begin{aligned} Q_{\pm,\omega,i,j} &= \int_0^T \left(e^{\pm is\lambda}\Pi_\omega\psi^2(T-s)\chi_0^2(x)\Pi_\omega e^{\mp is\lambda}(e_i)|e_j\right) ds \\ &= \int_0^T \psi^2(T-s)e^{\pm is(\omega_j-\omega_i)}\, ds\, \left(\chi_0^2 e_i|e_j\right). \end{aligned}$$

Since $\psi(t) \in C_0^\infty$ has support in $[0,T]$, we get that for any $k \in \mathbb{N}$, there exists a constant C_k, independent of the cutoff frequency ω, such that

$$\sup_{i,j} |(\omega_i-\omega_j)^k Q_{\pm,\omega,i,j}| \leq C_k. \qquad (2\text{–}26)$$

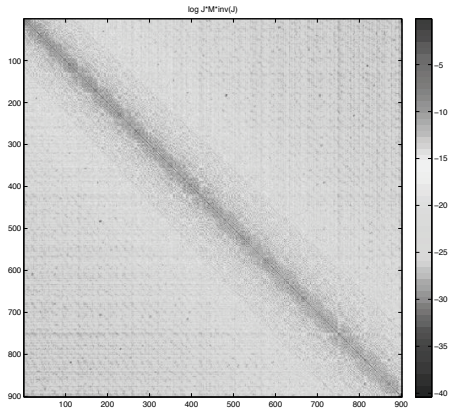

FIGURE 4. View of the logarithm of the coefficients of the matrix JM_TJ^{-1}, for the square geometry, with smooth control (zoom). This illustrates decay estimate (2–26).

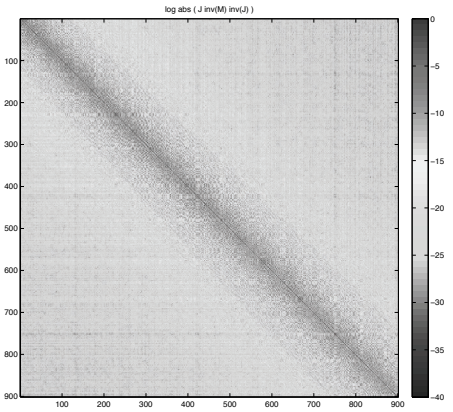

FIGURE 5. View of the logarithm of the coefficients of the matrix $JM_T^{-1}J^{-1}$, for the square geometry, with smooth control (zoom).

Moreover, by the results of [Dehman and Lebeau 09], we know that the operator $\mathcal{T}$ defined in (2–12) is smoothing, and therefore we get

$$\sup_{i,j} |(\omega_i + \omega_j)^k| \mathcal{T}_{\omega,i,j} \leq C_k. \tag{2–27}$$

Figure 3 (left) shows the logarithm of the coefficients of $JM_{T,\omega}J^{-1}$ and illustrates the decay estimates (2–26) and (2–27). A zoom into the figure is shown in Figure 4, so that we can observe more precisely (2–26). In particular, we can observe that the distribution of the coefficients along the diagonal of the matrix is not regular. Figure 5 presents the same zoom for $JM_{T,\omega}^{-1}J^{-1}$. This gives an illustration of the matrix structure of a microlocal operator. Figure 3 (right) represents the logarithm of the coefficients of $JM_{T,\omega}J^{-1}$ *without smoothing*. And finally, Figure 6 gives a view of the convergence of our Galerkin approximation by presenting the matrix entries of $J(\Lambda_\omega - M_{T,\omega}^{-1})J^{-1}$, illustrating Lemma 2.7, its proof, and Lemma 2.9.

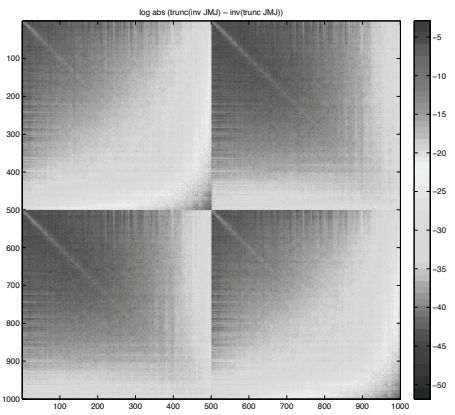

FIGURE 6. View of the logarithm of the coefficients of the matrix $J\left[((M_T)^{-1})_\omega - ((M_T)_\omega)^{-1}\right]J^{-1} = J\left[\Lambda_\omega - ((M_T)_\omega)^{-1}\right]J^{-1}$, for the square geometry, with smooth control. The M_T matrix is computed with 2000 eigenvalues, the cutoff frequency ω being associated with the 500th eigenvalue.

2.4 Computation of the Discrete Control Operator

For any real ω, let $N(\omega) = \sup\{n, \omega_n \leq \omega\}$. Then the dimension of the vector space L^2_ω is equal to $N(\omega)$. We define

$$\phi_j = \begin{cases} \frac{e_j}{\omega_j} & \text{for } 1 \leq j \leq N(\omega), \\ e_{j-N(\omega)} & \text{for } N(\omega)+1 \leq j \leq 2N(\omega). \end{cases} \tag{2–28}$$

Then $(\phi_j)_{1\leq j\leq 2N(\omega)}$ is an orthonormal basis of the Hilbert space $H_\omega = \Pi_\omega(H_0^1(\Omega) \oplus L^2(\Omega))$.

In this section we compute explicitly $\left(M_T\phi_l \mid \phi_k\right)_H$ for all $1 \leq k, l \leq 2N(\omega)$. We recall

$$e^{isA}\begin{bmatrix} e_i \\ 0 \end{bmatrix} = \begin{bmatrix} \cos(s\omega_i)e_i(x) \\ -\omega_i \sin(s\omega_i)e_i(x) \end{bmatrix},$$
$$e^{isA}\begin{bmatrix} 0 \\ e_i \end{bmatrix} = \begin{bmatrix} \sin(s\omega_i)e_i(x)/\omega_i \\ \cos(s\omega_i)e_i(x) \end{bmatrix}.$$

We now compute the coefficients of the M_T matrix, namely $M_{T\,n,m} = \left(M_T\phi_n \mid \phi_m\right)_H$:

$$\begin{aligned} M_{T\,n,m} &= \left(M_T\phi_n \mid \phi_m\right)_H \\ &= \int_0^T \left(e^{isA}BB^*e^{-isA}\phi_n \mid \phi_m\right)_H dt \\ &= \int_0^T \left(\begin{pmatrix} 0 & 0 \\ 0 & \chi^2 \end{pmatrix} e^{-isA}\phi_n \mid e^{-isA}\phi_m\right)_H dt. \end{aligned}$$

We now have to distinguish four cases, depending on m, n being smaller or larger than $N(\omega)$. For the case $(m, n) \leq N(\omega)$ we have

$$\begin{aligned} &M_{T\,n,m} \\ &= \int_0^T \left(\begin{pmatrix} 0 & 0 \\ 0 & \chi^2 \end{pmatrix} e^{-isA}\phi_n | e^{-isA}\phi_m\right)_H ds \\ &= \int_0^T \left(\begin{pmatrix} 0 & 0 \\ 0 & \chi^2 \end{pmatrix} \begin{bmatrix} \cos(s\omega_n)f_n(x) \\ \omega_n \sin(s\omega_n)f_n(x) \end{bmatrix} | \begin{bmatrix} \cos(s\omega_m)f_m(x) \\ \omega_m \sin(s\omega_m)f_m(x) \end{bmatrix}\right)_H ds \\ &= \int_0^T \left(\begin{bmatrix} 0 \\ \omega_n\chi^2 \sin(s\omega_n)f_n(x) \end{bmatrix} \mid \begin{bmatrix} l\cos(s\omega_n)f_m(x) \\ \omega_m \sin(s\omega_m)f_m(x) \end{bmatrix}\right)_H ds \\ &= \int_0^T \left((\psi(t)\chi_0(x))^2\omega_n \sin(s\omega_n)f_n(x) \right. \\ &\qquad \left. \mid \omega_m \sin(s\omega_m)f_m(x)\right)_{L^2(\Omega)} ds \\ &= \int_0^T \psi^2 \sin(s\omega_n)\sin(s\omega_m)\, ds \int_\Omega \chi_0^2 e_n(x)e_m(x)\, dx \\ &= a_{n,m}G_{n,m} \end{aligned}$$

where

$$a_{n,m} = \int_0^T \psi^2 \sin(s\omega_m)\sin(s\omega_n)\, ds \tag{2–29}$$

and

$$G_{n,m} = \int_\Omega \chi_0^2(x)\, e_m(x)\, e_n(x)\, dx. \tag{2–30}$$

Similarly, for the case $n > N(\omega)$, $m \leq N(\omega)$, we have

$$\begin{aligned} &M_{T\,n,m} \\ &= \int_0^T \left(\begin{pmatrix} ll0 & 0 \\ 0 & \chi^2 \end{pmatrix} e^{-isA}\phi_n | e^{-isA}\phi_m\right)_H ds \\ &= \int_0^T \left(\begin{pmatrix} ll0 & 0 \\ 0 & \chi^2 \end{pmatrix} \begin{bmatrix} l\sin(s\omega_n)f_n(x)/\omega_n \\ \cos(s\omega_n)f_n(x) \end{bmatrix} \right. \\ &\qquad \left. | \begin{bmatrix} l\cos(s\omega_m)f_m(x) \\ \omega_m \sin(s\omega_m)f_m(x) \end{bmatrix}\right)_H ds \\ &= \int_0^T \left(\begin{bmatrix} l0 \\ \chi^2\cos(s\omega_n)f_n(x) \end{bmatrix} | \begin{bmatrix} l\cos(s\omega_n)f_m(x) \\ \omega_m \sin(s\omega_m)f_m(x) \end{bmatrix}\right)_H ds \\ &= \int_0^T (\chi^2 \cos(s\omega_n)f_n(x) | \omega_m \sin(s\omega_m)f_m(x))_{L^2(\Omega)}\, ds \\ &= \int_0^T \psi^2 \cos(s\omega_n)\sin(s\omega_m)\, ds \int_\Omega \chi_0^2 e_n(x)e_m(x)\, dx \\ &= b_{n,m}G_{n,m}, \end{aligned}$$

where

$$b_{n,m} = \int_0^T \psi^2 \cos(s\omega_n)\sin(s\omega_m)\, ds. \tag{2–31}$$

For $n \leq N(\omega)$ and $m > N(\omega)$ we get

$$M_{T\,n,m} = c_{n,m}G_{n,m},$$

where

$$c_{n,m} = b_{m,n} = \int_0^T \psi^2 \cos(s\omega_m)\sin(s\omega_n)\, ds, \tag{2–32}$$

And for $m, n > N(\omega)$, we have

$$M_{T\,n,m} = d_{n,m}G_{n,m},$$

where

$$d_{n,m} = \int_0^T \psi^2 \cos(s\omega_m)\cos(s\omega_n)\, ds. \tag{2–33}$$

The above integrals have to be implemented carefully when $|\omega_n - \omega_m|$ is small, even when $\psi(t) = 1$.

3. NUMERICAL SETUP AND VALIDATION

3.1 Geometries and Control Domains

The code we implemented allows us to choose the two-dimensional domain Ω, as well as the control domain U. In the sequel, we will present some results with three different geometries: square, disk, and trapezoid. For each geometry, we have chosen a reference shape of control domain. It consists of the neighborhood of two adjacent sides of the boundary (in the square), of a radius (in the disk), or of the base side (in the trapezoid). Then we adjust the width of the control domain, and also its smoothness (see next subsection). Figures 7, 8, and 9 present these domains, and their respective control domains, either nonsmooth (left panels) or smooth (right panels).

3.2 Time and Space Smoothing

We will investigate the influence of the regularity of the function $\chi(t, x) = \psi(t)\chi_0(x)$. Different options have been set.

3.2.1 Space Smoothing. The integral (2–30) defining $G_{n,m}$ features χ_0. In the literature we find $\chi_0 = \mathbf{1}_U$, so that

$$G_{n,m} = \int_U e_n(x)\, e_m(x)\, dx.$$

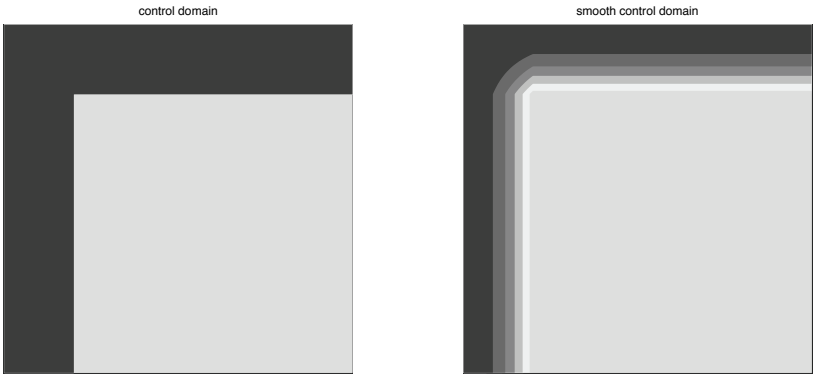

FIGURE 7. Domain and example of a control domain for the square, with smoothing in space (right panel) or without (left panel).

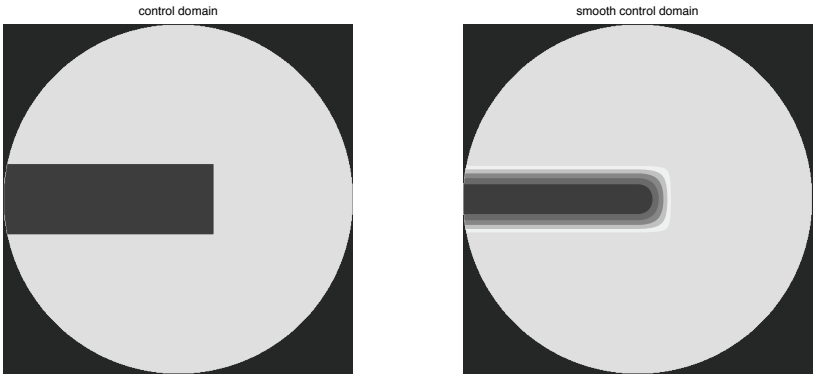

FIGURE 8. Domain and example of a control domain for the disk, with smoothing in space (right panel) or without (left panel).

In [Dehman and Lebeau 09] the authors show that a smooth χ_0^2 leads to a more regular control (see also Theorem 2.4 and Lemma 2.9). Thus for each control domain U we implemented both smooth and nonsmooth (constant) cases. The different implementations of χ_0 are as follows:

- constant case: $\chi_0(x,y) = \mathbf{1}_U$,
- "smooth" case: $\chi_0(x,y)$ has the same support of U, the width a of the domain $\{x \in \Omega, 0 < \chi_0(x) < 1\}$ is adjustable, and on this domain χ is a polynomial of degree 2. For example, in the square we have

$$\begin{aligned}\chi_0(x,y) &= \mathbf{1}_U\Big[1 - \Big(\mathbf{1}_{x\geq a} + \frac{x^2}{a^2}\cdot \mathbf{1}_{x<a}\Big) \\ &\qquad \times \Big(\mathbf{1}_{y\leq 1-a} + \frac{(1-y)^2}{a^2}\cdot \mathbf{1}_{y>1-a}\Big)\Big].\end{aligned} \tag{3–1}$$

3.2.2 Time Smoothing. Similarly, the time integrals (2–29), (2–31), (2–32), (2–33) defining a, b, c, and d fea-

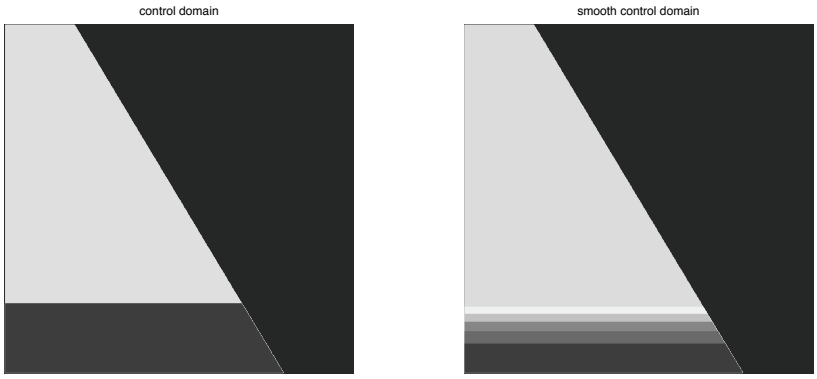

FIGURE 9. Domain and example of a control domain for the trapezoid, with smoothing in space (right panel) or without (left panel).

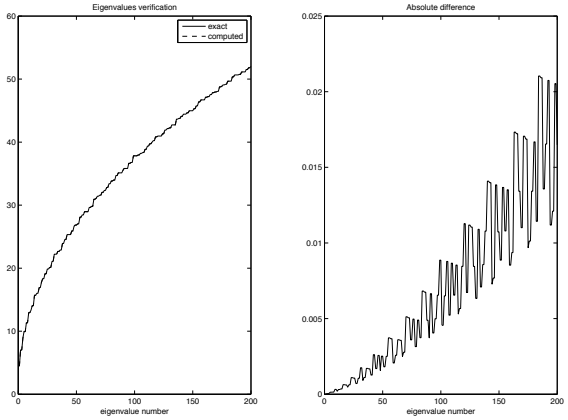

FIGURE 10. Verification of the eigenvalue computation in the square: exact and finite-differences-computed eigenvalues (left panel), and their absolute difference (right panel).

ture $\psi(t)$, which is commonly chosen as $\mathbf{1}_{[0,T]}$. As previously, better results are expected with a smooth $\psi(t)$. In the code, the above-mentioned integrals are computed explicitly, with the different implementations of ψ as follows:

- constant case $\psi = \mathbf{1}_{[0,T]}$,
- "smooth case"

$$\psi(t) = \frac{4t(T-t)}{T^2}\mathbf{1}_{[0,T]}. \qquad (3\text{–}2)$$

3.3 Validation of the Eigenvalue Computation

The code we implemented has a wide range of geometries for Ω. Since it is a spectral Galerkin method, it requires the accurate computation of eigenvalues and eigenvectors. We used the Matlab function `eigs`. Figure 10 presents a comparison between the first 200 exact eigenvalues in the square and those computed by Matlab with 500×500 grid points. Figure 11 presents the same comparison in the disk, for 250 eigenvalues, the "exact" ones being computed as zeros of a Bessel function.

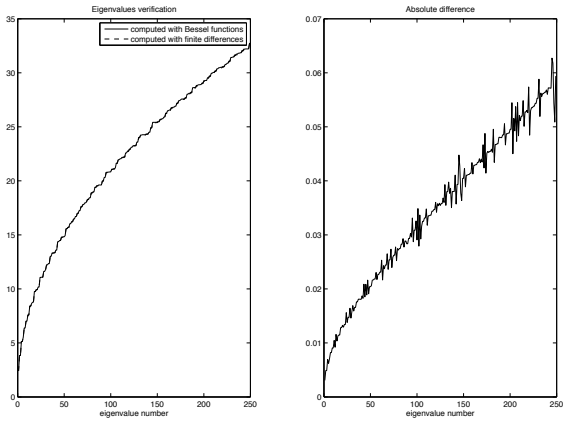

FIGURE 11. Verification of the eigenvalue computation in the disk: eigenvalues computed either as zeros of Bessel functions or with finite differences (left panel), and their absolute difference (right panel).

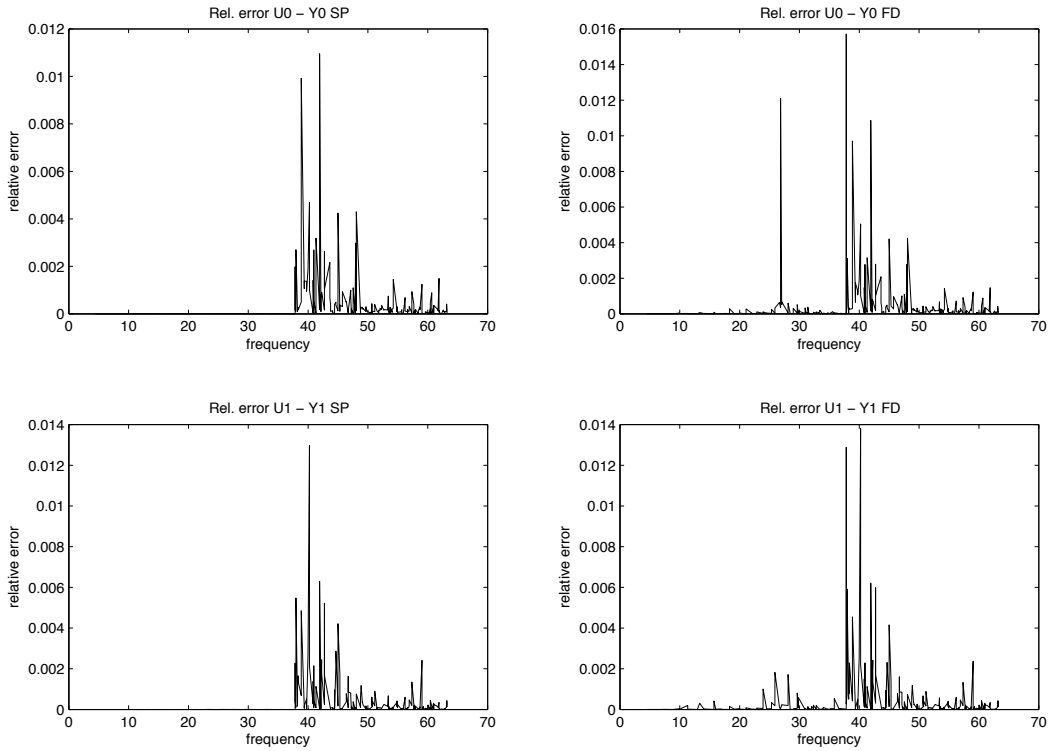

FIGURE 12. Validation experiments in the square: Relative errors between the spectral coefficients of the original function u and the reconstructed function y, computed with exact eigenvalues (left panels) or finite differences eigenvalues (right panels), for u_0 and y_0 (top panels) or u_1 and y_1 (bottom panels). The errors are plotted as a function of the frequency of the eigenvalues. The computation are performed with 100 eigenvalues, corresponding to a frequency of about 38, the reconstruction with 2000, corresponding to a frequency of about 160. For the readability of the figure, we plot only the major counterparts of the error, i.e. we stop the plot after frequency 63 (300th eigenvalue).

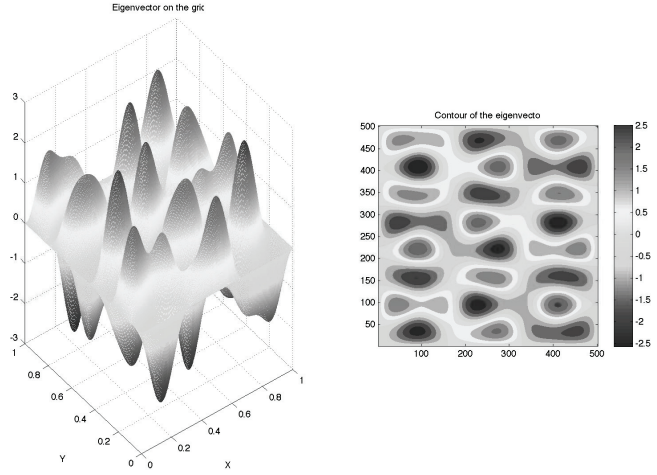

FIGURE 13. Representation on the grid in 3D (left panel) and contour plot (right panel) of the fiftieth eigenvector in the square.

3.4 Reconstruction Error

In the sequel, we will denote the input data by $u = (u_0, u_1)$ and its image by the control map $w = (w_0, w_1) = \Lambda(u_0, u_1)$, which will often be called the *control*. We recall from Section 2.1 that for given data $u = (u_0, u_1)$ to be reconstructed at time T, the optimal control $v(t)$ is given by

$$v(t) = \chi \partial_t e^{-i(T-t)A} w = \chi \partial_t e^{-i(T-t)A} \Lambda(u).$$

Then solving the wave equations (2–2) forward, with null initial conditions and χv as a forcing source, we reach $y = (y_0, y_1)$ in time T. If the experiment were perfect, we would have $(y_0, y_1) = (u_0, u_1)$. The reconstruction error is then by definition

$$E = \sqrt{\frac{\|u_0 - y_0\|^2_{H^1(\Omega)} + \|u_1 - y_1\|^2_{L^2(\Omega)}}{\|u_0\|^2_{H^1(\Omega)} + \|u_1\|^2_{L^2(\Omega)}}}. \qquad (3\text{–}3)$$

3.5 Validation for the Square Geometry

3.5.1 Finite Differences versus Exact Eigenvalues. We compare various outputs for our spectral method when the eigenvalues and eigenvectors are computed either with finite differences or with exact formulas. In our first experiment, we have $N \times N = 500 \times 500$ grid points, and we use $N_e = 100$ eigenvalues to compute the G and M_T matrices. The data (u_0, u_1) are as follows:

$$u_0 = e_{50}, \quad u_1 = 0, \qquad (3\text{–}4)$$

where e_n denotes the nth *exact* eigenvector. A representation of the 50th eigenvector e_{50} of the square can be found in Figure 13. The control time T is equal to 3, the control domain U has width 0.2, and we do not use any smoothing. For reconstruction we use 2000 eigenvalues and eigenvectors.

Table 1 shows the condition number of the M_T matrices and reconstruction errors, which are very similar for both experiments.

Figure 12 shows the relative reconstruction errors SP_n and FD_n between the data u and the reconstructed y for both experiments:

$$\mathrm{SP}_n = \frac{|U_{0,n} - Y^{sp}_{0,n}|}{\|U_0 + U_1\|}, \quad \mathrm{FD}_n = \frac{|U_{0,n} - Y^{fd}_{0,n}|}{\|U_0 + U_1\|},$$

and similarly for u_1 and y_1, where $U_{0,n}$ is the nth spectral coefficient of the data u_0, $Y^{sp}_{0,n}$ is the nth spectral coefficient (in the basis (ϕ_j) defined by (2–28)) of the reconstructed y_0 when the control w is obtained using exact eigenvalues, and $Y^{fd}_{0,n}$ is the nth spectral coefficient of y_0 when the control w is obtained using finite difference eigenvalues. The norm $\|U_0 + U_1\|$ in our basis (ϕ_j) is given by $\|U_0 + U_1\|^2 = \sum_{n=1}^{N_e} U^2_{0,n} + U^2_{1,n}$. For exact eigenvalues, we can see that the errors are negligible for the first hundred spectral coefficients, and quite small on the next ones. We have similar results for finite difference eigenvalues, except that we have an error at the fiftieth coefficient.

This error does not occur when the reconstruction is done with the same basis of finite difference eigenvectors, and it can probably be explained as follows: to compute the reconstructed y from the finite difference control w, we first compute an approximation of w as a function of (x, y) (i.e., on the grid) from its spectral coefficients (on the basis of finite difference eigenvectors); then we compute the coefficients of this function on the exact basis (thanks to a very simple integration formula).

We thus introduce two sources of error—projection on the grid and projection on the exact basis—that do not have anything to do with our spectral Galerkin method. Therefore we will not discuss the matter in further detail here.

Eigenvalue Computation	Condition Number	Reconstruction Error
Finite differences	7.4	1.8 %
Exact	7.5	1.6 %

TABLE 1. Validation experiments in the square: Condition numbers and validation errors for a 100-eigenvalue experiment in the square (without smoothing), where the eigenvalues are exact or computed using finite differences.

3.5.2 Impact of the Number of Eigenvalues. In this subsection, we still use the same data (3–4), but the number of eigenvalues and eigenvectors N_e used to compute the M_T matrices varies. Table 2 shows M_T condition numbers and reconstruction errors for various N_e with exact or finite-difference-computed eigenvalues. The reconstruction is still performed with 2000 exact eigenvalues. We can see that the finite difference eigenvalues lead to almost as good results as exact eigenvalues. We also observe in both cases the decrease of the reconstruction error with an increasing number of eigenvalues, as predicted in Lemma 2.9. A five-percent error is obtained with 70 eigenvalues (the input data being the fiftieth eigenvalue), and using 100 eigenvalues leads to an error of less than two percent.

	Condition Number		Reconstruction Error	
N_e	Exact	Finite Differences	Exact	Finite differences
52	6.5	6.4	29.2%	29.0%
55	6.6	6.6	17.7%	17.6%
60	6.6	6.6	17.3%	17.2%
70	7.1	7.0	4.9%	5.0%
80	7.3	7.2	3.2%	3.3%
100	7.5	7.4	1.6%	1.8%
200	8.3	8.3	0.5%	1.0%
300	8.8		0.3%	
500	9.5		0.2%	

TABLE 2. Validation experiments in the square: Condition numbers and validation errors for various numbers N_e of eigenvalues used to compute the control function, where the eigenvalues are exact or computed using finite differences. The input data is the fiftieth eigenvalue, and the reconstruction is performed with 2000 eigenvalues.

4. NUMERICAL EXPERIMENTS

4.1 Frequency Localization

In this subsection, the geometry (square) as well as the number of eigenvalues used (200 for HUM, 2000 for verification) are fixed. Note also that in this subsection we use only exact eigenvalues for HUM and verification.

The data are also fixed to a given eigenmode, that is,

$$u_0 = e_{50}, \quad u_1 = 0,$$

where e_n is the nth eigenvector of $-\Delta$ on the square.

The first output of interest is the spreading of w spectral coefficients, compared to u. Figure 14 shows the spectral coefficients of the input (u_0, u_1) and the control (w_0, w_1) with and without smoothing. As predicted by Theorem 2.4 and Lemma 2.9, we can see that the main coefficient of (w_0, w_1) is the fiftieth of w_0, and also that the smoothing noticeably improves the localization of w.

Similarly we can look at the spectral coefficients of the reconstruction error. Figure 15 presents the reconstruction error (see Section 3.4 for a definition) with or without smoothing. We notice that the errors occur mostly above the cutoff frequency (used for the computation of $M_{T,\omega}$, and thus for the control computation). Another important remark should be made here: the smoothing has a spectacular impact on the frequency localization of the error, as well as on the absolute value of the error (maximum of 2×10^{-3} without smoothing and 8×10^{-7} with smoothing), as announced in Theorem 2.4 and Lemma 2.9.

Remark 4.1. For other domains, such as the disk and trapezoid, as well as other one-mode input data, we obtain similar results. The results also remain the same if we permute $u0$ and $u1$, i.e., if we choose $u0 = 0$ and $u1$ equal to one fixed mode.

4.2 Space Localization

4.2.1 Dirac Experiments. In this section we investigate localization in space. To do so, we use "Dirac" functions $\delta_{(x,y)=(x_0,y_0)}$ as data, or more precisely truncations of Dirac functions to a given cutoff frequency:

$$u_0 = \sum_{i=1}^{N_i} e_n(x_0, y_0)\, e_n, \quad u_1 = 0,$$

where N_i is the index corresponding to the chosen cutoff frequency, with $N_i = 100$ or 120 in the sequel. Figure 16 shows the data u_0 and the control w_0 in the square with exact eigenvalues, without smoothing, the results being similar with smoothing. We can see that the support of w_0 is very similar to that of u_0. Figure 17 presents the reconstruction error associated with this experiment. We can see as before that the smoothing produces highly reduced errors.

Similarly, we performed experiments with numerical approximation of a Dirac function as input data in the disk and in a trapezoid. Figures 18 and 19 present the space localization of u_0 and w_0 without smoothing (we get similar results with smoothing). As previously, the control w_0 is supported by roughly the same area as the input u_0. In the disk we can see a small disturbance, located in the symmetric area of the support of u_0 with respect to the control domain U. However, this error does not increase with N_i, as we can see in Figure 20 (case $N_i = 200$), so it remains compatible with Conjecture 2.5.

Figure 21 shows the reconstruction errors for these experiments, with or without smoothing. As before, we notice the large improvement produced by the smoothing. We get similar errors in the trapezoid.

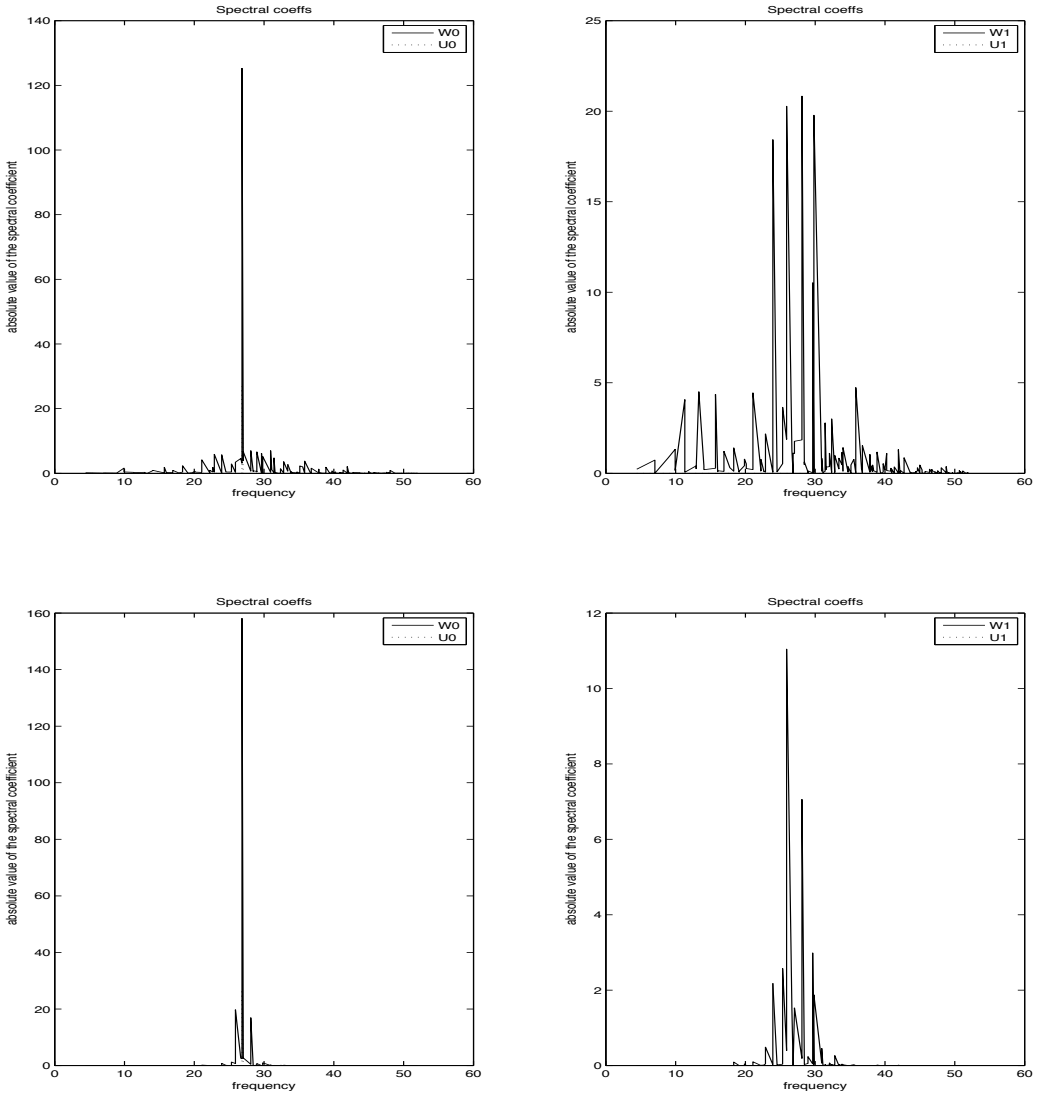

FIGURE 14. One-mode experiment in the square: localization of the Fourier frequencies of (u_0, u_1) (dashed line) and (w_0, w_1) (solid line) for a given time T and a given domain U without smoothing (top) and with time and space smoothing (bottom). The x-coordinate represents the eigenvalues. The input data u_0 is equal to the fiftieth eigenvector, equal to an eigenvalue of about 26.8, and $u_1 = 0$.

4.2.2 Box Experiments in the Square. In this subsection we consider the case $u_0 = \mathbf{1}_{\text{box}}$, where

$$\text{box} = [0.6, 0.8] \times [0.2, 0.4]$$

is a box in the square. The control domain U has width 0.1: $U = \{x < 0.1 \text{ and } y > 0.9\}$. These experiments were performed in the square with 1000 exact eigenvalues for the M_T matrix computation, the input data u_0 being defined using 800 eigenvalues. Figures 22 and 23 show the space localization of the data u_0 and the control w_0 without and with smoothing. As before, we can observe that the space localization is preserved, and that with smoothing the support of w_0 is more sharply defined.

Figures 24 and 25 show the reconstruction errors for two different data, the first being the same as in Figure 22, and the second being similar but rotated by $\pi/4$. We show here only the case with smoothing, the errors being larger but similarly shaped without. We can observe that the low and high values of the errors are located on a lattice whose axes are parallel to the box sides. This is compatible with the structure of the wave-front set associated with both input data.

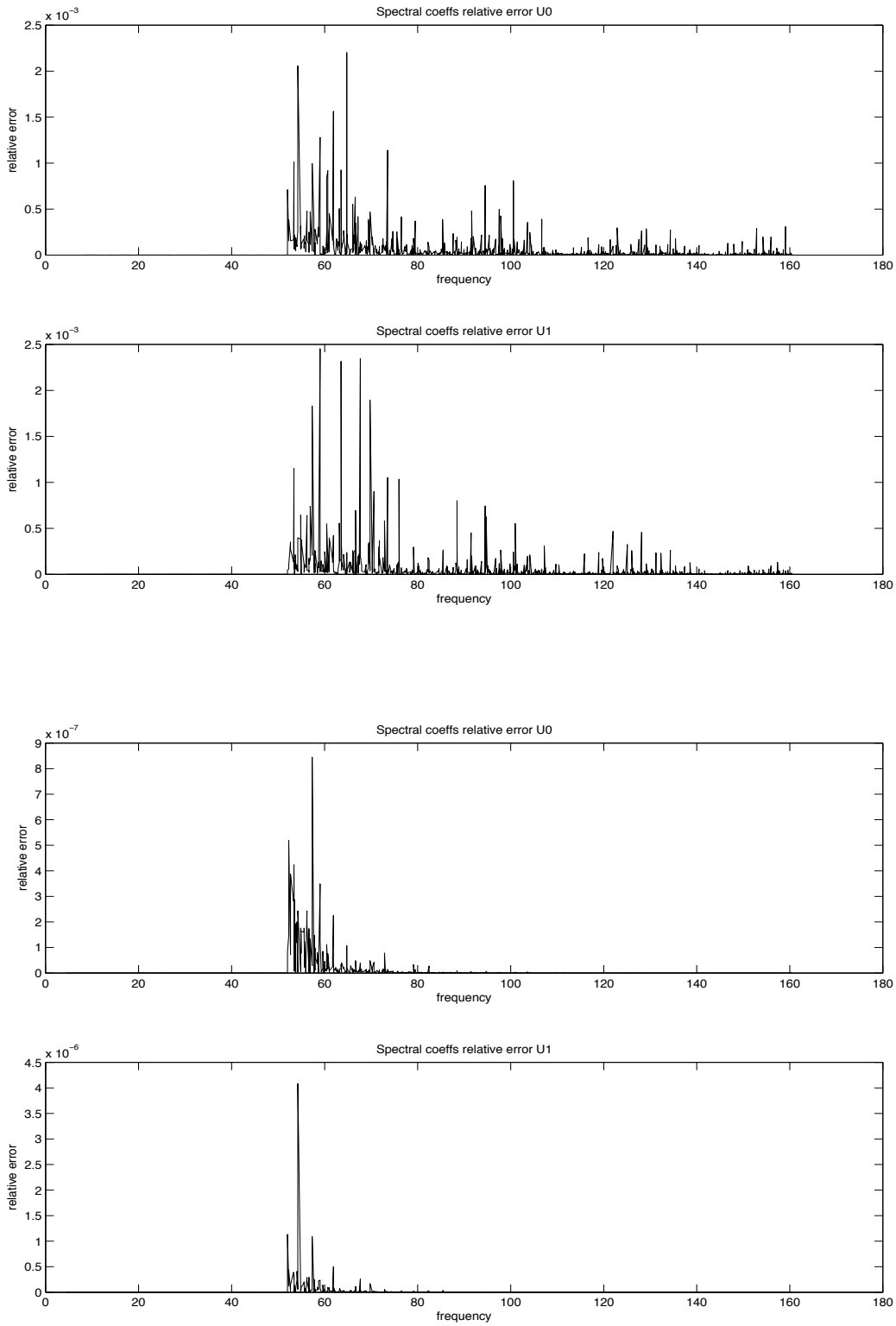

FIGURE 15. One-mode experiment in the square: localization of the Fourier coefficients of $(u_0 - y_0, u_1 - y_1)$, where u is the data and y is the reconstructed function obtained from the control function w, for a given time T and a given domain U without smoothing (top panels) and with time and space smoothing (bottom panels).

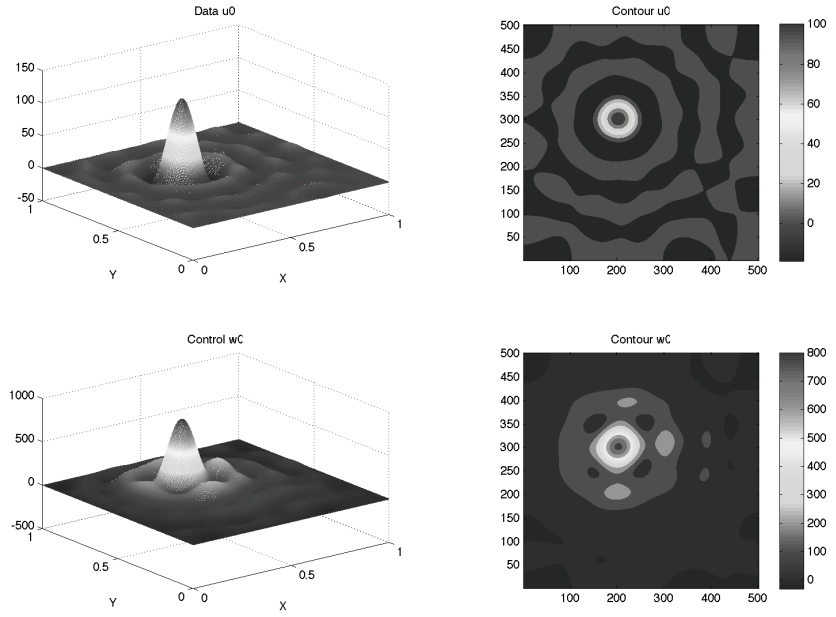

FIGURE 16. Space localization of the data u_0 (top panels) and the control w_0 (bottom panels), for a Dirac experiment in the square, with exact eigenvalues. These plots correspond to an experiment without smoothing, but it is similar with smoothing. Left panels represent a 3D view, and right panels show contour plots.

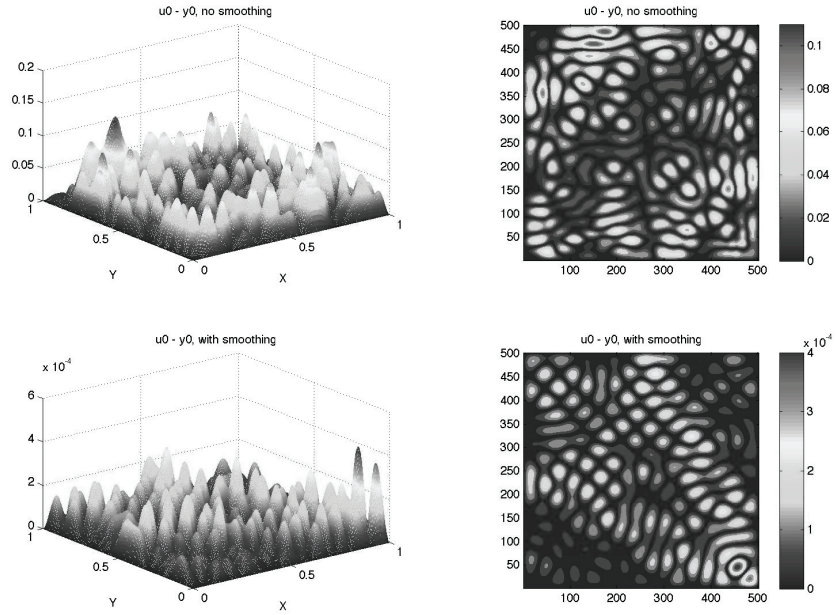

FIGURE 17. Difference between the data u_0 and the reconstructed function y_0 without smoothing (top panels) and with smoothing (bottom panels) for a Dirac experiment in the square, with exact eigenvalues. Left panels represent 3D view, and right panels show contour plots.

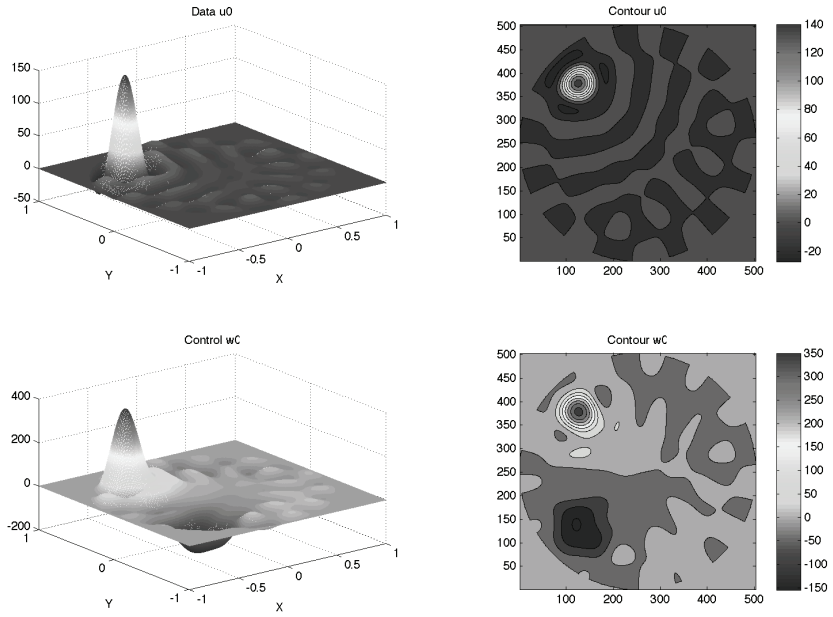

FIGURE 18. Space localization of the data u_0 (top panels) and the control w_0 (bottom panels) for a Dirac experiment in the disk. These plots correspond to an experiment without smoothing, but the results are similar with smoothing. Left panels represent a 3D view, and right panels show contour plots. In this experiment, the input data are defined with $N_i = 100$ eigenvectors.

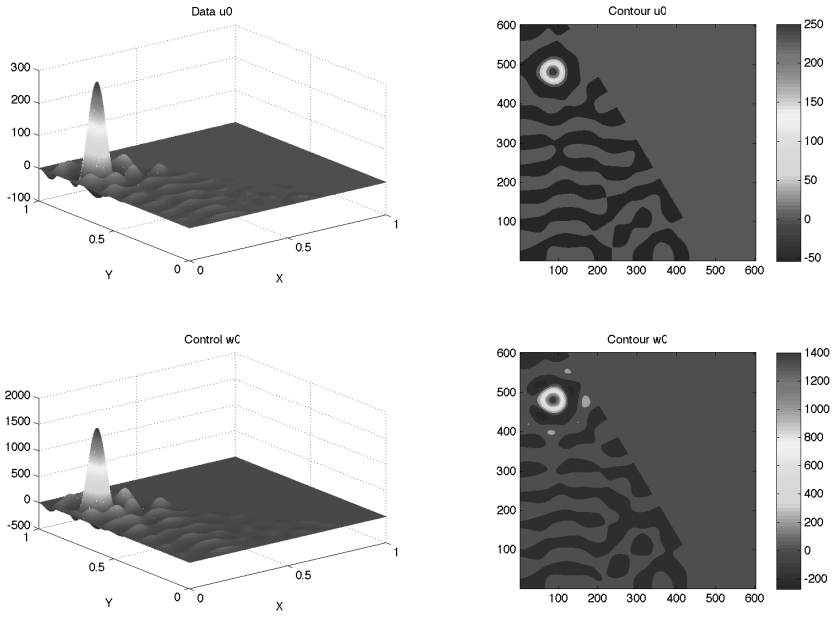

FIGURE 19. Space localization of the data u_0 (top panels) and the control w_0 (bottom panels) for a Dirac experiment in the trapezoid. These plots correspond to an experiment without smoothing, but the results are similar with smoothing. Left panels represent a 3D view, and right panels show contour plots. In this experiment, the input data are defined with $N_i = 120$ eigenvectors.

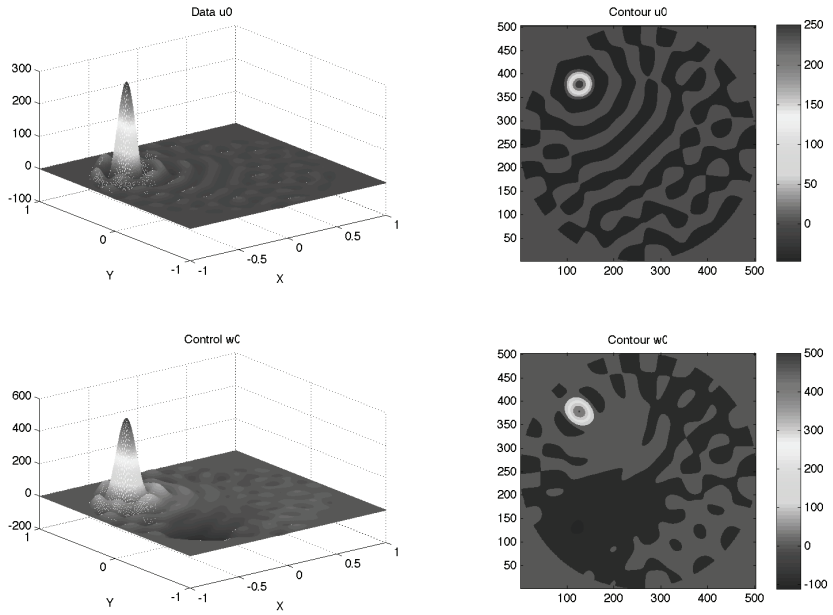

FIGURE 20. Space localization of the data u_0 (top panels) and the control w_0 (bottom panels) for a Dirac experiment in the disk. These plots correspond to an experiment with smoothing, and the results are similar without smoothing. Left panels represent a 3D view, and right panels show contour plots. In this experiment, the input data are defined with $N_i = 200$ eigenvectors.

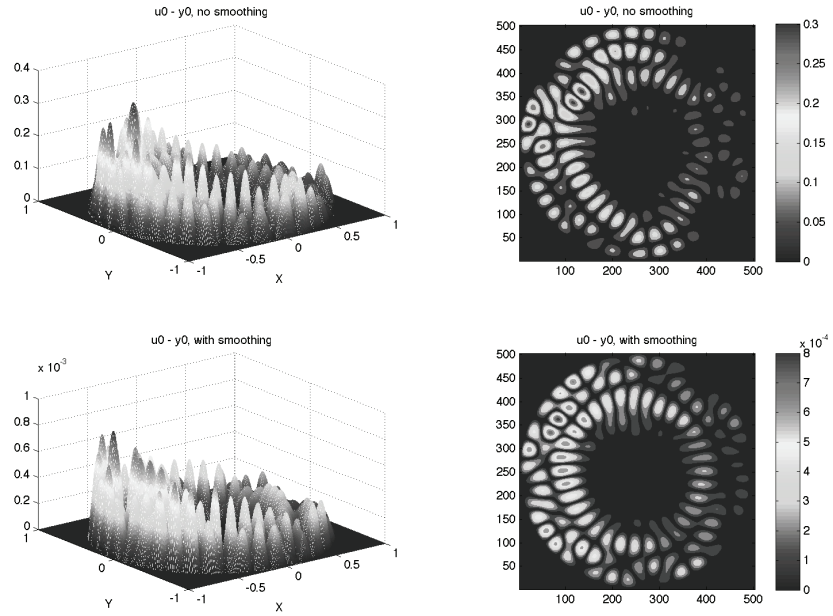

FIGURE 21. Difference between the data u_0 and the reconstructed function y_0 for a Dirac experiment in the disk without smoothing (top panels) and with time and space smoothing (bottom panels). Left panels represent a 3D view, and right panels show contour plots. In this experiment, the input data are defined with $N_i = 100$ eigenvectors.

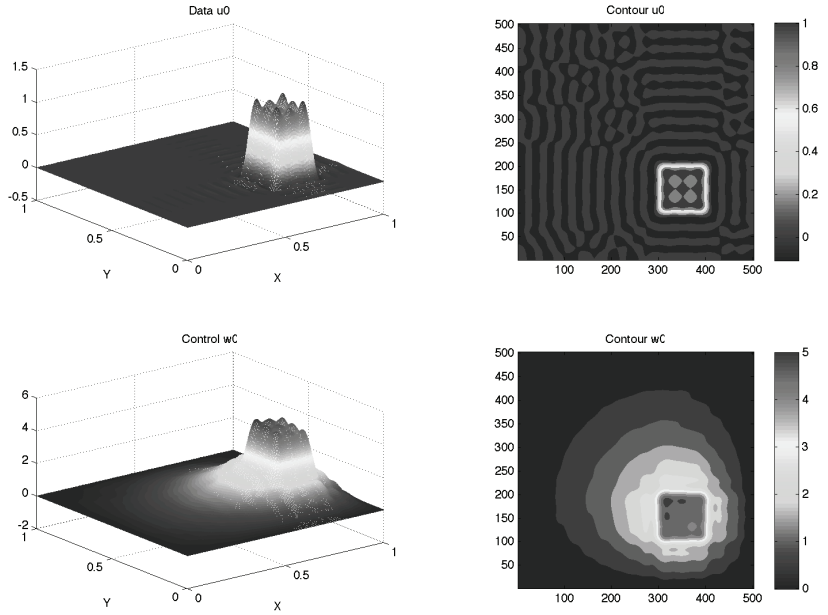

FIGURE 22. Space localization of the control function w_0 (bottom panels) with respect to the data u_0 (top panels), in the square, without smoothing: 3D plots on the left, and contour plots on the right.

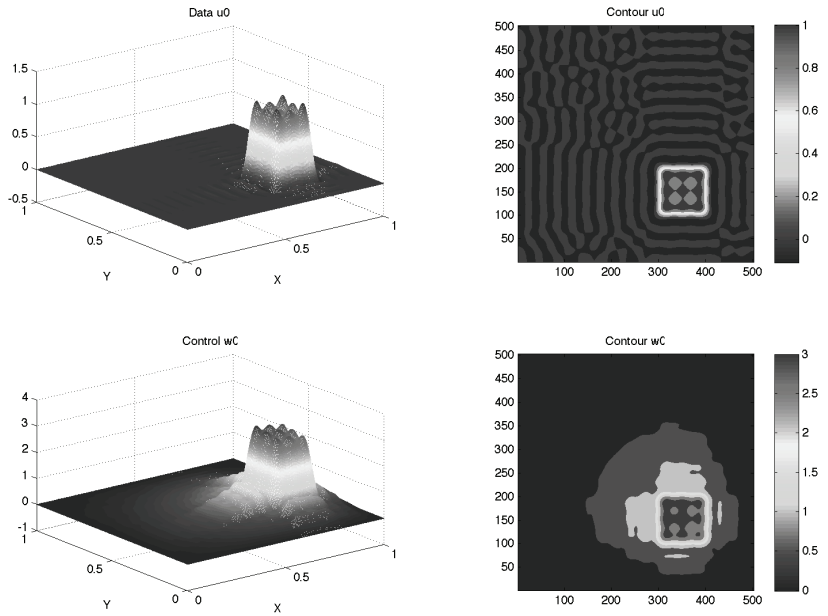

FIGURE 23. Space localization of the control function w_0 (bottom panels) with respect to the data u_0 (top panels), in the square, with smoothing. Left panels represent a 3D view, and right panels show contour plots.

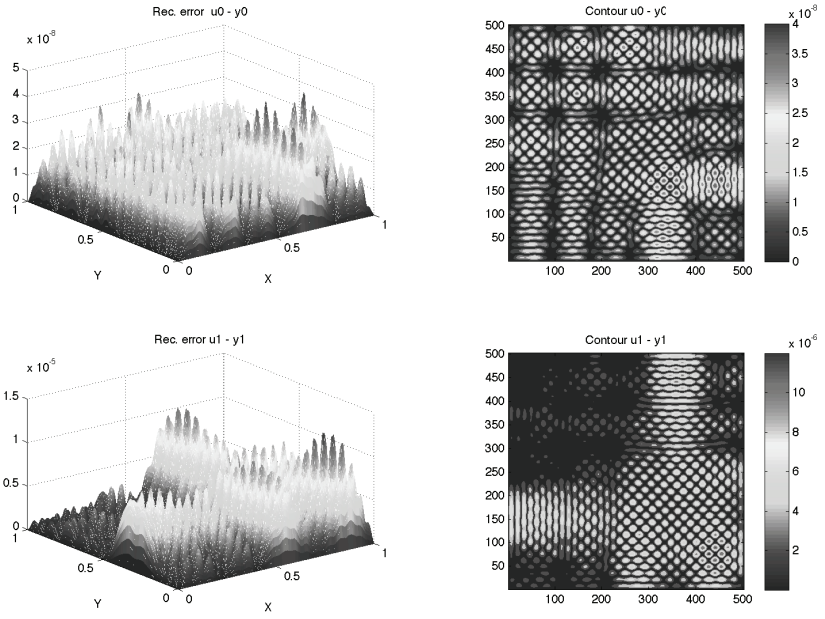

FIGURE 24. Difference between the data u_0 and the reconstructed function y_0 (top panels) and u_1 and y_1 (bottom panels) with smoothing in the square. The data is the identity function of a square whose edges are parallel to the x and y axes. Left panels represent a 3D view, and right panels show contour plots.

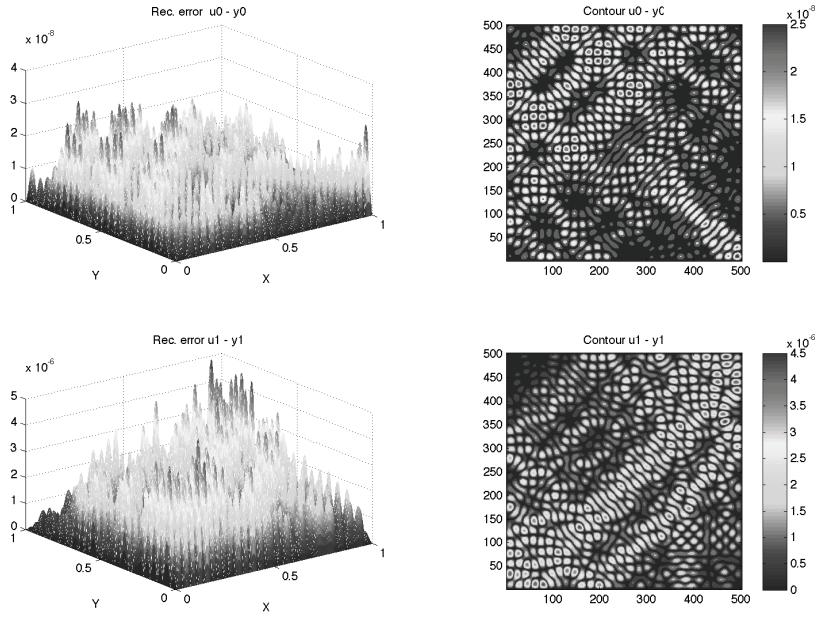

FIGURE 25. Difference between the data u_0 and the reconstructed function y_0 (top panels) and u_1 and y_1 (bottom panels) with smoothing in the square. The data is the identity function of a square whose edges are parallel to the diagonals of the square. Left panels represent a 3D view, and right panels show contour plots.

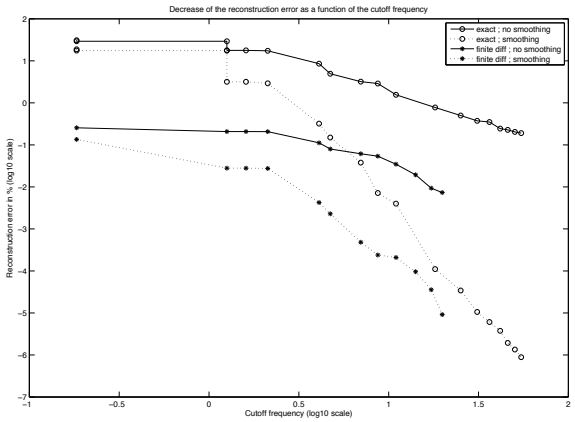

FIGURE 26. Reconstruction errors for the finite differences and exact methods, as a function of the cutoff frequency (i.e., the largest eigenvalue used for the control computation), with and without time and space smoothing.

4.3 Reconstruction Error

In this section we investigate Lemma 2.9. This lemma states that the reconstruction error should decrease faster than any polynomial if the function $\chi(t,x)$ is smooth. So we would like to compare the decrease for both our choices of χ, and we expect to get a a slow decrease for the classical choice of the function χ (i.e., not smooth), and a faster decrease with the smooth function (see Section 3.2 for details about smooth/not smooth). To investigate this, we perform a "one-mode" experiment (see Section 4.1) using the fiftieth mode as input data. We then compute the control with an increasing cutoff frequency, up to 160 (finite differences case) or 500 (exact case), and we compute the reconstruction error, thanks to a larger cutoff frequency (200 in the finite differences case and 2000 in the exact case).

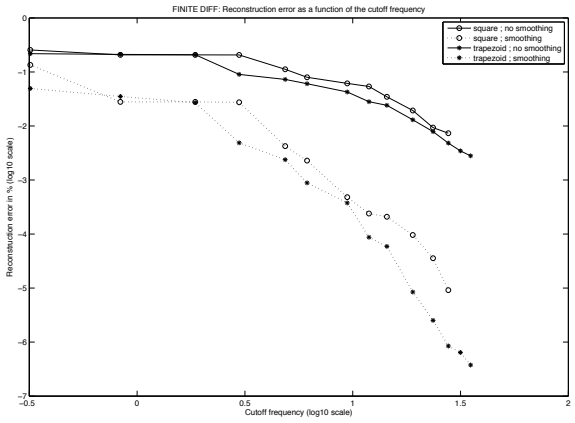

FIGURE 27. Reconstruction errors for the finite difference method, in the square and in the trapezoid, as a function of the cutoff frequency (i.e., the largest eigenvalue used for the control computation), with or without time and space smoothing.

Figure 26 represents the reconstruction error (with exact or finite differences eigenvalues) as a function of the cutoff frequency (i.e., the largest eigenvalue used for the control function computation). Figure 27 presents the same results (with finite difference eigenvalues only) for two different geometries: the square and the trapezoid (general domain). The log scale allows us to see that the error actually decreases as the inverse of the cutoff frequency without smoothing, and as the inverse of the fifth power of the cutoff frequency with smoothing.

4.4 Energy of the Control Function

In this subsection we investigate the impact of smoothing, the width of the control domain U and the control time T on various outputs such as the condition number of M_T, the reconstruction error $\|u-y\|$, and the norm of the control function $\|w\|$.

To this end, we performed several one-mode experiments (see Section 4.1, mode 500) in the square, with exact eigenvalues, 1000 eigenvalues used for computation of M_T, 2000 eigenvalues used for reconstruction and verification. We chose various times, 2.5 and 8, plus their "smoothed" counterparts, according to the empirical formula $T_{\text{smooth}} = \frac{15}{8}T$. This increase of T_{smooth} is justified on the theoretical level by formulas (2–14) and (2–13), which show that the efficiency of the control is related to a mean value of $\chi(t,x)$ on the trajectories. Similarly, we chose various widths of U: 1/10 and 3/10, plus their "smoothed" counterparts, which are double. Table 3 presents the numerical results for these experiments. This table requires several remarks. First, the condition number of M_T, the reconstruction error, and the norm of the control w decrease with increasing time and U. Second, if we compare each nonsmooth experiment with its "smoothed" counterpart (the comparison is of course approximate, since the "smoothed" time and width formulas are only reasonable approximations), the condition number seems similar, as well as the norm of the control function w, whereas the reconstruction error is far smaller with smoothing than without.

Figures 28 and 29 emphasize the impact of the control time. They present the reconstruction error, the norm of the control, and the condition number of M_T as a function of the control time (varying between 2.5 and

Smooth	Width of U	Time	Condition Number	Rec. Error	$\|w\|$
no	1/10	2.5	48.8303	0.00518843	504.287
yes	2/10	2.5	204.048	0.00140275	1837.12
yes	2/10	4.7	21.7869	4.65892E-07	364.013
no	1/10	8	21.1003	0.00162583	120.744
yes	2/10	8	16.5497	8.51442E-08	189.361
yes	2/10	15	12.017	8.39923E-09	100.616
no	3/10	2.5	4.20741	0.0014823	147.009
yes	6/10	2.5	9.05136	1.94519E-06	336.704
yes	6/10	4.7	3.09927	2.99855E-08	125.481
no	3/10	8	3.20921	0.000488423	39.9988
yes	6/10	8	2.74172	6.0204E-09	69.8206
yes	6/10	15	2.4113	8.55119E-10	37.1463

TABLE 3. Impact of the control time, the width of U and the smoothing, on the condition number of M_T, on the reconstruction error, and on the norm of the control function. These results come from one-mode experiments in the square, with exact eigenvalues.

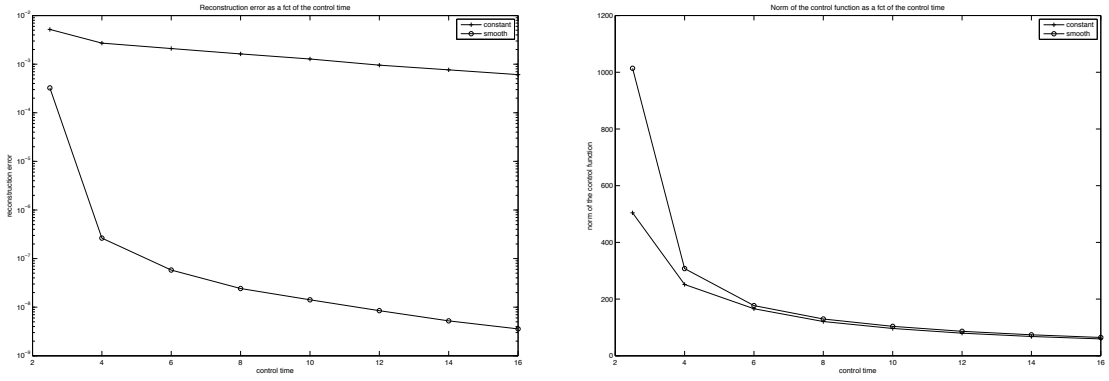

FIGURE 28. Experiments in the square, with exact eigenvalues: impact of the smoothing on the reconstruction error (left) and on the norm of the control function (right), as a function of the control time.

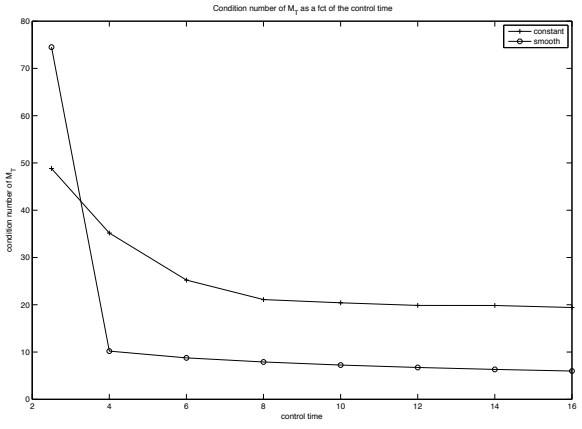

FIGURE 29. Experiments in the square, with exact eigenvalues: impact of smoothing on the condition number of the M_T matrix, as a function of the control time.

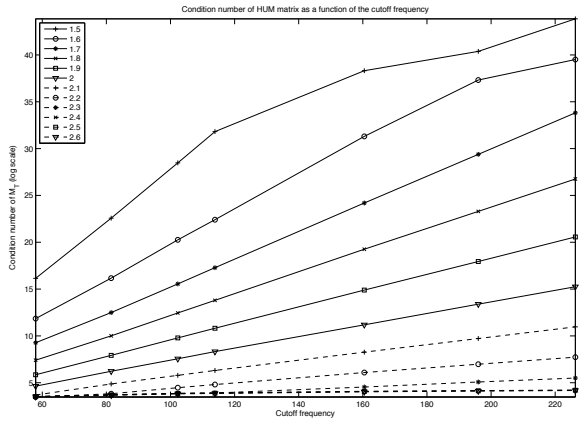

FIGURE 30. Condition number of the $M_{T,\omega}$ matrix as a function of the cutoff frequency ω for various control times.

16), with or without smoothing. Conclusions are similar to those given in the table.

4.5 Condition Number

In this section, we investigate Conjecture 2.8. To do so, we compute the condition number of $M_{T,\omega}$, since we have

$$\mathrm{cond}(M_{T,\omega}) = \|M_{T,\omega}\| \cdot \|M_{T,\omega}^{-1}\| \simeq \|M_T\| \cdot \|M_{T,\omega}^{-1}\|.$$

Figure 30 shows the condition number of the M_T matrix as a function of the control time or of the last eigenvalue used for the control function computation. According to

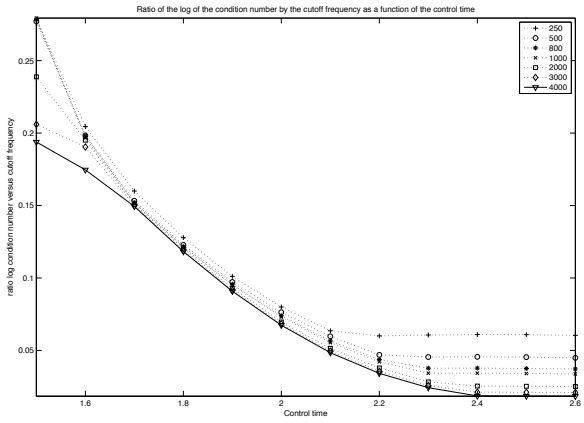

FIGURE 31. Ratio of the log of the condition number of the $M_{T,\omega}$ matrix and the cutoff frequency ω as a function of the control time for various numbers of eigenvalues.

Conjecture 2.8, we obtain lines of the type

$$\log\left(\mathrm{cond}(M_{T,\omega})\right) = \omega \cdot C(T,U).$$

Figure 31 shows for various numbers of eigenvalues the following curves:

$$T \mapsto \frac{\log\left(\mathrm{cond}(M_{T,\omega})\right)}{\omega}.$$

Similarly, we can draw conclusions compatible with Conjecture 2.8, since these curves seem to converge as the number of eigenvalues grows to infinity.

4.6 Noncontrolling Domains

In this section we investigate two special experiments with noncontrolling domains, i.e., such that the geometric control condition is not satisfied regardless of the control time.

First we consider the domain presented in Figure 32. For this domain the condition number of the M_T matrix is large, and consequently, we should be experiencing difficulties to reconstruct the data u. We perform one-mode experiments with two different eigenvectors, one localized in the center of the disk (eigenvalue 60), the other localized around the boundary (eigenvalue 53), as can be seen in Figure 33.

The various outputs are presented in Table 4, and we can see that the inversion is fairly accurate for the 53rd eigenmode, while it is logically poor for the 60th eigenmode. Moreover, the energy needed for the control process, i.e., the norm of the control w, is small for the 53rd eigenvector, while it is large for the 60th. We can also notice that the smoothing has the noticeable effect of decreasing the reconstruction error, the norm of the control function w being similar.

In the second experiment we change the point of view: instead of considering one given domain and two different data, we consider one given data and two different noncontrolling domains. The data is again u_{53} (see Figure 33), which is localized at the boundary of the disk. The first domain is the previous one (see Figure 32), and the second domain is presented in Figure 34; it is localized at the center of the disk.

In either case, the condition number of the M_T matrix is large, and the data should prove difficult to reconstruct. Table 5 presents the outputs we obtained for the two domains. As previously, we observe that the control process works fairly well for the appropriate control domain, with a small error as well as a small energy for the control. Conversely, when the control domain does not "see" the input data, the results are poorer: the energy

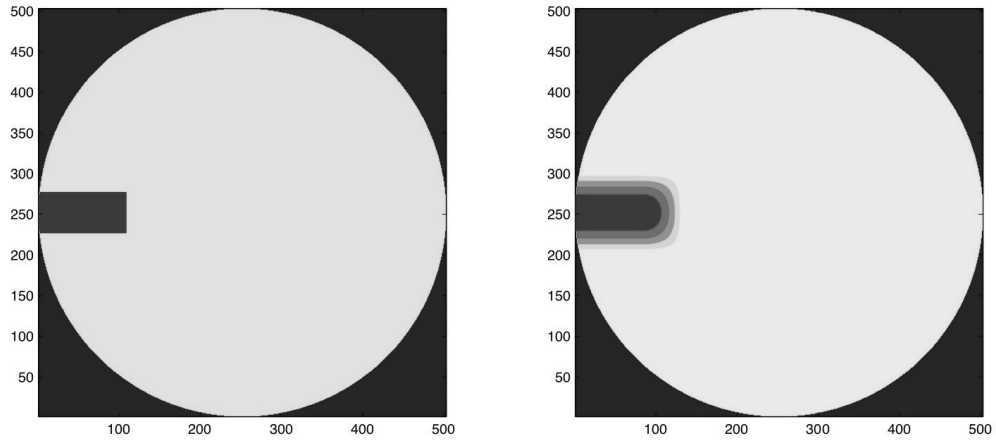

FIGURE 32. Noncontrolling domain U without (left) and with (right) smoothing. This domain consists of the neighborhood of a radius that is truncated around the disk boundary.

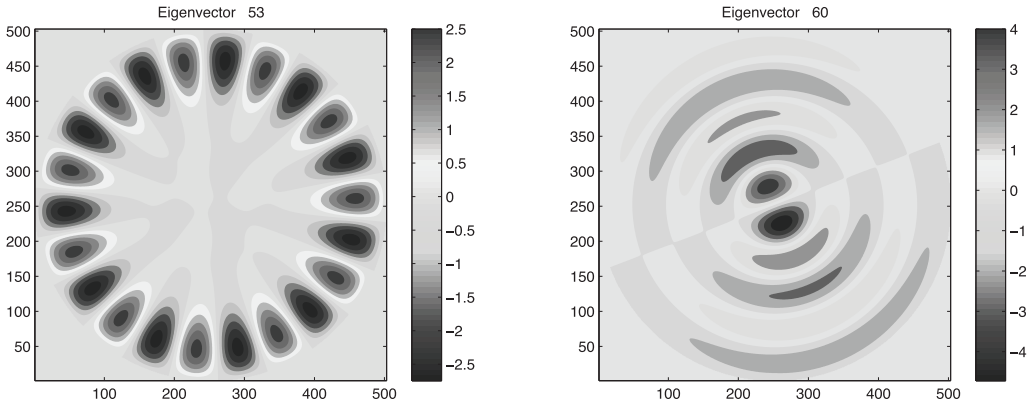

FIGURE 33. Special modes chosen for experiment with noncontrolling domains, corresponding to the 53rd and 60th eigenvalues.

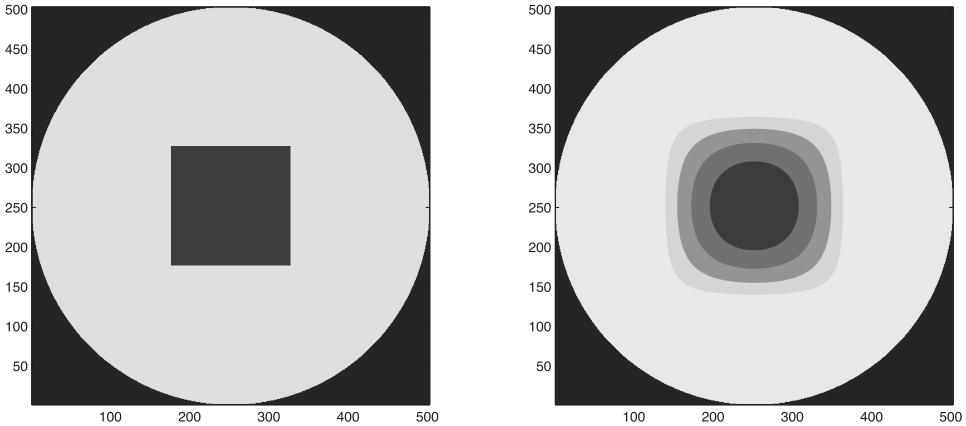

FIGURE 34. Noncontrolling domain U without (left) and with (right) smoothing. This domain consists of the neighborhood of a radius that is truncated around the disk center.

Smooth?	Condition Number	53rd Eigenmode Rec. Error	$\|w\|$	60th Eigenmode Rec. Error	$\|w\|$
no	4960	0.63%	15	26%	4583
yes	6042	6.5×10^{-4}%	24	0.11%	8872

TABLE 4. Influence of the shape of the data on the reconstruction error and the norm of the control, with a noncontrolling domain U. On the left, the 53rd eigenmode is localized around the boundary of the circle, as is the control domain. On the right, the 60th eigenmode is localized around the center of the circle.

Smooth?	First Domain Cond. Number	Rec. Error	$\|w\|$	Second Domain Cond. Number	Rec. Error	$\|w\|$
no	4960	0.63%	15	3.6×10^6	68%	1.9×10^4
yes	6042	6.5×10^{-4}%	24	3.3×10^5	9.4×10^{-3}%	6.5×10^5

TABLE 5. Reconstruction error and the norm of the control with data u_{53} localized at the boundary of the disk and two different noncontrolling domains U, the first one localized around the boundary, the second one around the center.

needed is large with or without smoothing, and the error is also large without smoothing. It is, however, small with smoothing.

ACKNOWLEDGMENTS

The experiments in this paper were realized with Matlab software on computers at Laboratoire Jean-Alexandre Dieudonné (Nice) and Laboratoire Jean Kuntzmann (Grenoble). The INRIA Gforge was also used. The authors thank J.-M. Lacroix (Laboratoire J.-A. Dieudonné) for his management of the Nice computing machine. This work has been partially supported by Institut Universitaire de France.

REFERENCES

[Asch and Lebeau 98] M. Asch and G. Lebeau. "Geometrical Aspects of Exact Boundary Controllability of the Wave Equation: A Numerical Study." *ESAIM:COCV* 3 (1998), 163–212.

[Burq and Lebeau 01] N. Burq and G. Lebeau. "Mesures de défaut de compacité, application au système de lamé." *Ann. Sci. École Norm. Sup.* 34:6 (2001), 817–870.

[Bardos et al. 92] C. Bardos, G. Lebeau, and J. Rauch. "Sharp Sufficient Conditions for the Observation, Control and Stabilisation of Waves from the Boundary." *SIAM J. Control Optim.* 305 (1992), 1024–1065.

[Dehman and Lebeau 09] B. Dehman and G. Lebeau. "Analysis of the HUM Control Operator and Exact Controllability for Semilinear Waves in Uniform Time." To appear in *SIAM Control and Optimization*, 2009.

[Gérard 91] P. Gérard. "Microlocal Defect Measures." *C.P.D.E.* 16 (1991), 1762–1794.

[Glowinski et al. 90] R. Glowinski, C. H. Li, and J.-L. Lions. "A Numerical Approach to the Exact Boundary Controllability of the Wave Equation (I). Dirichlet Controls: Description of the Numerical Methods." *Japan J. Appl. Math.* 7 (1990), 1–76.

[Glowinski et al. 08] R. Glowinski, J. W. He, and J.-L. Lions. *Exact and Approximate Controllability for Distributed Parameter Systems: A Numerical Approach.* Cambridge, UK: Cambridge University Press, 2008.

[Hörmander 85] L. Hörmander. *The Analysis of Linear Partial Differential Operators, III*, Grundl. Math. Wiss. 274. Berlin: Springer, 1985.

[Lebeau 92] G. Lebeau. "Contrôle analytique I : Estimations a priori." *Duke Math. J.* 68:1 (1992), 1–30.

[Lions 88] J.-L. Lions. *Contrôlabilité exacte, perturbations et stabilisation de systèmes distribués. Tome 2*, Recherches en Mathématiques Appliquées [Research in Applied Mathematics] 9. Paris: Masson, 1988.

[Melrose and Sjöstrand 78] R.-B. Melrose and J. Sjöstrand. "Singularities of Boundary Value Problems I." *CPAM*, 31 (1978), 593–617.

[Melrose and Sjöstrand 82] R.-B. Melrose and J. Sjöstrand. "Singularities of Boundary Value Problems II." *CPAM* 35 (1982), 129–168.

[Russell 78] D.-L. Russell. "Controllability and Stabilizability Theory for Linear Partial Differential Equations: Recent Progress and Open Questions." *SIAM Rev.* 20 (1978), 639–739.

[Taylor 81] M. Taylor. *Pseudodifferential Operators.* Princeton: Princeton University Press, 1981.

[Zuazua 02] E. Zuazua. "Controllability of Partial Differential Equations and Its Semi-discrete Approximations." *Discrete and Continuous Dynamical Systems* 8:2 (2002), 469–513.

[Zuazua 05] E. Zuazua. "Propagation, Observation, and Control of Waves Approximated by Finite Difference Methods." *SIAM Rev.* 47:2 (2005), 197–243.

Gilles Lebeau, Université de Nice, Institut Universitaire de France, Laboratoire J.-A. Dieudonné, Parc Valrose, Nice, France (lebeau@math.unice.fr)

Maëlle Nodet, Université de Grenoble, INRIA, Laboratoire J. Kuntzmann, Domaine Universitaire, Grenoble, France (maelle.nodet@inria.fr)

Received September 9, 2008; accepted March 3, 2009.